THREE-DIMENSIONAL NONEQUILIBRIUM VISCOUS SHOCK-LAYER FLOWS OVER COMPLEX REENTRY VEHICLES

by

S. Swaminathan

Dissertation submitted to the Faculty of the
Virginia Polytechnic Institute and State University
in partial fulfillment of the requirements for the degree of
DOCTOR OF PHILOSOPHY
in
Aerospace Engineering

APPROVED:

Dr. C. H. Lewis, Chairman

Dr. J. A. Schetz

Dr. J. F. Marchman, III

Dr. A. K. Jakubowski

Dr. D. T. Mook

May, 1983
Blacksburg, Virginia

THREE-DIMENSIONAL NONEQUILIBRIUM VISCOUS SHOCK-LAYER FLOWS OVER COMPLEX REENTRY VEHICLES

by

S. Swaminathan

(ABSTRACT)

A computer program for predicting the three-dimensional nonequilibrium viscous shock-layer flows over blunt sphere-cones, straight and bent multiconics at angle-of-attack has been developed. The method used is the viscous shock-layer approach for nonequilibrium, multi-component ionizing air. A seven species chemical reaction model with single ionizing species and an eleven species chemical reaction model with five ionizing species are used to represent the chemistry. The seven species model considers 7 reactions whereas the eleven species model considers 26, reactions and the results obtained using these models are compared with perfect gas and equilibrium air results. This code is capable of analyzing shock-slip or no-shock-slip boundary conditions and equilibrium or non-catalytic wall boundary conditions. In this study the diffusion model is limited to binary diffusion.

A sphere-cone-cylinder-flare with moderate flare angle, a straight biconic, and a bent biconic with seven deg. bend

angle and a sphere-cone at various flight conditions are analyzed using this method. The bent biconic has been analyzed up to an angle-of-attack of 20 deg. with respect to the aft-cone axis and sample results are compared with inviscid and viscous results. The surface pressure distribution computed by this code compares well with that from a parabolized Navier-Stokes method. The diffusion heat transfer is about 15% of the total heat transfer for most cases. The aerodynamic forces and moments at the base of the body and computing time required for all cases are presented. The shock layer profiles at a streamwise location of 8.8 nose radii for one case computed using seven and eleven species models compare very well with each other.

ACKNOWLEDGEMENTS

The author wishes to thank Dr. C. H. Lewis who, as the Chairman of his Advisory Committee, has given constant encouragement and guidance in this research work.

The author also wishes to thank Dr. J. A. Schetz, Dr. J. F. Marchman III Dr. A. K. Jakubowski and Dr. D. T. Mook for their review and suggestions on the thesis. The author is thankful to Dr. W. L. Neu for agreeing to substitute for Dr. D. T. Mook during the final examination and for his suggestions and review on the thesis.

This research is part of a project from National Aeronautical and Space Administration at Langley. Special thanks are due to for the discussions on the various aspects of the project. The author wishes to thank for all the administrative and typing help.

Finally the author wishes to thank his wife, , for her patience and moral support.

TABLE OF CONTENTS

Appendix

LIST OF TABLES

LIST OF FIGURES

NOMENCLATURE

A_0 - A_5 =Coefficients of the parabolic partial differential equations

ALFA =Angle of attack

CA =Axial Force coefficient

CFPINF =Skin-friction coefficient in the transverse directions

CFSINF =Skin-friction coefficient in the streamwise directions

CI =Denotes C_i

C_i =Concentration of species i, ρ_i/ρ

CM =Pitching moment coefficient about the nose tip

CN =Normal force coefficient

Cp =Specific heat at constant pressure

$\hat{C}_{pi}$ =Species specific heat

D_j =Binary diffusion coefficient

E-/CC =Electron concentration per cubic centimeter

ECW =Equilibrium catalytic wall

EQBM =Chemical equilibrium

FCW =Fully catalytic wall

H =Stagnation enthalpy , H^*/U_∞^2

$\hat{H}_i$ =Species specific enthalpy

h =Static enthalpy, h^*/U_∞^2

h_1, h_2, h_3 =Shape factors for a general orthogonal coordinite system

J_i =Diffusion mass flow term

k =Thermal conductivity,

k_{br} =Backward rate constant

k_{fr} =Forward rate constant

L =Length of the vehicle, m

Le =Lewis number

M_∞ =Mach number

M =Species molecular weight

$\overline{M}$ =Mixture molecular weight

NCW =Noncatalytic wall

NEQ =Finite rate nonequilibrium chemical reactions

NJ =Number of species plus catalytic third bodies, NS+NZ

NR =Number of chemical reactions

NS =Number of species

NSH =Shock stand-off distance, n_{sh}

NSHP = $\frac{\partial n_{sh}}{\partial \xi}$

NSS =Denotes no shock slip

NZ =Number of catalytic third bodies

PG =Perfect gas

PHI =Circumferential coordinate

PINF =Freestream pressure

Pr =Prandtl number

PW =Wall pressure

p =Pressure, $p^* / \rho_\infty U^2_\infty$

q_w =Heat-transfer rate at the wall

R =Gas constant, ft^2/sec^2 R

Re =Reynolds number,

Rn* =Nose radius, m

RN =Denotes Rn*

SORN =s*/Rn*

SP =Denotes species

SS =Denotes shock slip

STINF =Stanton number , $q_w^* / \rho_\infty U_\infty (H_0^* - H_w^*)$

s,n,ϕ =Nondimensional surface-oriented coordinate system

T =Temperature, $T^*/T_{ref} = T^*/(\gamma-1) T_\infty M_\infty^2$

U_∞ =Freestream velocity, m/sec

u,v,w =Velocity components, u^* / U_∞, v^* / U_∞, w^* / U_∞

W =Dependent variable

$\dot{w}_i$ =Species production term

Y =Distance normal to body

ZCP =Center-of-pressure location measured from nose tip, m

ZORN =z/Rn*

z =Axial length

α =Angle of attack, deg

ε =Reynolds number parameter, $\varepsilon^2 = \mu_{ref}/\rho_\infty U_\infty R_n^*$

γ =Ratio of specific heats

μ =Viscosity , μ^*/μ_{ref}

ξ, η, ζ =Normalized surface-oriented coordinates

ρ =Density, ρ^*/ρ_{ref}

σ =Shock angle

α =Stoichiometric coefficients for reactants

β =Stoichiometric coefficients for products

Superscripts

(-) =Normalized variable

( ) =Denotes shock-normal coordinate system

* =Dimensional variable

(=) =Measured from base of the body

Subscripts

eq =Equilibrium value

i =Species i

ref =Dimensional reference conditions

w =Wall conditions

∞ =Dimensional freestream conditions

sh =Conditions behind the bow shock

ζ =Derivative with respect to ζ

0 =Stagnation conditions

Chapter I

INTRODUCTION

The viscous shock-layer equations, because of their advantages and their accurate predictions with reasonable cost, are widely used as a tool for engineering calculations. These equations treat the entire flowfield from the body to the bow shock in an uniform manner, and hence the displacement effects and the outer boundary conditions can be accurately modelled. The governing partial differential equations are parabolic in both streamwise and crossflow directions, and this makes solutions far downstream on long reentry vehicles possible with reasonable expense. The low densities encountered at high altitudes cause low Reynolds numbers which make the classical inviscid/boundary-layer approach difficult to use. These advantages of the viscous shock-layer equations inspired many investigators to apply the viscous shock-layer equations for more complicated problems.

In recent years, increased interest is being shown in the aerobraking and aerocapture techniques, and this introduces the problem of analysis of flowfields over complex shapes such as multiconics and bent biconics. Since aerobraking and aerocapture are performed at relatively high altitudes,

the vehicle is in a chemical nonequilibrium flow regime for most of the time. Also, during aerocapture the vehicle is operating at reasonably high angles-of-attack. This necessitates the analysis of multiconics and bent biconics in three-dimensional nonequilibrium flow. The perfect gas flows over multiconics and bent biconics have been analyzed by earlier investigators. Nevertheless, three-dimensional, nonequilibrium flow has not been analyzed by any previous investigator for these complex configurations.

Davis[1] solved the shock-layer equations for laminar perfect gas flows over analytic bodies and Srivastava, Werle and Davis[2] treated the problem of curvature discontinuity on a sphere-cone. Miner and Lewis[3,4] treated a seven-species air mixture consisting of N, O, N2, O2, NO, NO+ and e- with finite-rate chemical reactions over non-analytic blunt bodies such as sphere-cones at zero lift. Three-dimensional perfect gas flowfields with wall slip were analyzed by Murray and Lewis.[5,6] Szema and Lewis[7] extended the three-dimesional viscous shock-layer method to include laminar, transitional and/or turbulent shock-layer flows. Thareja, Szema and Lewis[8] studied the effects of chemical equlibrium on the three-dimensional viscous shock-layer analysis of hypersonic laminar or turbulent flows. Many investigators have studied the perfect gas flows over multiconics and bent biconics,

and to cite one recent study, Miller and Gnoffo[9,10] measured the surface pressure distribution over wind tunnel models of straight and bent biconics and compared the results from the predictions by various perfect gas (γ = 1.4) codes.

One of the main purposes of this paper is to study nonequilibrium three-dimensional flowfields over sphere-cones at angle-of-attack. This study was conducted in order to develop a code to predict, to a fair accuracy, the surface-measurable quantities over a sphere-cone and to provide initial-data plane profiles for a code for analyzing the nonequilibrium flow over the windward side of space shuttle, and all of this within reasonable computing time. The temperatures involved in reentry flowfields are very high and they cause dissociation and ionization of atmospheric molecules. Ionization affects transport phenomena and at higher entry speeds radiative transfer and communications as well. Since the reentry speeds of the space shuttle are not high enough to cause communication blackout, the concentration of the electrons in the shock layer was considered to be of secondary importance. Hence some simplifications were assumed during the preliminary study. Seven species ionizing air is considered as the medium, and it is assumed that the chemical reactions proceed at finite rate. Since the behaviour of electrons in the shock layer was of secondary impor-

tance, the electron temperature was assumed to be the same as that of the heavy particles.

From previous studies it has been observed that the assumption of binary diffusion with constant Lewis-Semenov numbers gives a reasonably accurate solution of surface-measurable quantities. Also Blottner's study[11] of nonequilibrium, laminar boundary-layer flow of ionized air showed that the electron density was slightly changed with the simpler diffusion model. The inclusion of multicomponent diffusion would increase the computing time considerably, and hence multicomponent diffusion and the effects of ambipolar diffusion were not included in this study.

Secondly the above code has been modified to analyze configurations used in the aero-assisted orbital transfer vehicles such as multiconics and bent biconics. The multiconics include straight biconics with expansion corners and a sphere-cone-cylinder-flare with a compression corner. The fluid medium is assumed to be a seven species air mixture consisting of N, O, N2, O2, NO, NO+, and e- and the chemical reactions are assumed to proceed at finite rates. The code is capable of treating shock slip and noncatalytic wall conditions.

The high velocities at which the aero-assisted orbital transfer vehicles fly generate very high temperatures, and the ionization of oxygen and nitrogen atoms and molecules at these temperatures has to be considered. Hence the above code has been modified to include an eleven-species chemical model with four additional ionizing species, viz. N+, O+, N2+ and O2+. In this model 26 reactions are considered.

The validation of the code has been done in steps. Initially the results for a 9 degree half-angle sphere-cone at zero angle-of-attack from the seven species model is compared with those from an earlier axisymmetric code (VSL7S)[3,4] and with RAM C flight test results. Because of a lack of three-dimensional nonequilibrium results, the results for non-zero angles-of-attack have been compared with those only from a perfect gas/equilibrium air code (VSLET)[8] and for some cases with the results from a parabolized Navier-Stokes method.[12] The surface pressure distributions predicted by the present method are compared with those computed by an inviscid finite-difference code (NOL3D).[13,14] The results from the eleven-species model have been compared with those from the seven-species model and flight data.

Chapter II

DESCRIPTION OF TEST CASES AND FREESTREAM CONDITIONS

Four different geometries were considered as test cases for this study. A nine-degree half-angle sphere-cone is used as a test case for verifying the new method. This geometry is analyzed at zero angle of attack, and the results are compared with those from an earlier axisymmetric code (VSL7S). The nose radius is 0.1524 m (6 inches) and the length of the cone is 20 nose radii. The analysis is performed at a freestream condition of 83.82 km (275 kft) and a freestream velocity of 7620 m/sec (25000 ft/sec). The freestream conditions are given in Table 1. The wall temperature is assumed to be 1000 K (1800 R). This case is also analyzed at a lower altitude of 70.1 km (230 kft) to see the effects of changes in altitude.

The second body is a 9/4 biconic with a nine-degree half-angle sphere-cone as the forebody (Fig. 1). The nose radius is 0.1524 m (6 inches), and the length of the forecone is 10 nose radii. The afterbody is a four-degree half-angle cone, and the total length of the body is 20 nose radii. A freestream velocity of 7620 m/sec (25,000 ft/sec) and 83.82 km (275 kft) altitude conditions are used for this

case. The wall temperature is maintained constant at 1000 K (1800R). The third geometry is a sphere-cone-cylinder-flare (Fig. 2) with a 9 degree sphere-cone as the forebody. The cylindrical portion is 10 nose radii long. The flare angle is 5 deg., and the flare length is 10 nose radii. The free-stream conditions for this case are the same as those for the biconic. A schematic of the forth geometry, a bent bi-conic, is shown in Fig. 3. This geometry is similar to those being proposed for the Titan probe or the Aeroassisted Orbital Transfer Vehicle (AOTV). The forecone is a 12.84 degree half-angle sphere-cone with a nose radius of 0.2 me-ters (0.66 feet). The aftcone is a seven-degree half-angle cone, and the total length is 30.4 nose-radii. The forecone axis is bent upwards by 7 deg. with respect to the aftcone axis. This causes a 12.84 deg. expansion on the windward side and a one deg. compression on the leeward side. The wall temperature in this case is assumed to be 555.5 K (1000R).

Chapter III

ANALYSIS

The three-dimensional shock-layer equations are developed in a body-oriented orthogonal coordinate system. (Fig. 4) The derivation of these equations is described in detail in Ref. 5 and 6 and hence is not discussed here. In this chapter, the boundary conditions, the sources of thermodynamic and transport properties and the chemical reaction model used for the analysis are discussed. A brief discussion on the modifications necessary for treating the geometrical discontinuities is also presented.

3.1 GOVERNING EQUATIONS

The viscous shock-layer equations are developed in a body-oriented orthogonal coordinate system (s,n,ϕ) where the s-coordinate is tangent to the body in the streamwise direction, n is the coordinate normal to the surface and the ϕ-coordinate is the angle around the body measured from the windward streamline (see Fig. 4). The shock-layer equations derive from the governing equations for reacting gas mixtures, given by Bird, Stewart and Lightfoot[15], and Williams.[16] These equations are first non-dimensionalized by variables which are of order one in the region near the body

surface and in the inviscid region. The normal velocty v and the normal coordinate n are assumed to be of order ε, and up to second-order terms are retained in the conservation equations. The equations are then normalized by the local shock values of the variables to aid in the solution procedure. To avoid division by small numbers, the normal and crossflow velocities (v and w), the temperature and species concentration are not normalized. The energy and species equations include the rate of production terms ($\dot{w}_i$ for species i) which are functions of both temperature and species concentrations. These terms are rewritten so that either temperature or species concentration appears as one of the unknowns. The complete set of equations are given in Appendix A.

3.2 BOUNDARY CONDITIONS

At the body surface, the no-slip boundary conditions were imposed. The surface conditions are

$$\tilde{u} = v = w = 0 \text{ and } T = T_w$$

where Tw is either a constant or a specified temperature variation. For a noncatalytic surface, (NCW), the species boundary conditions are

$$\frac{\partial C_i}{\partial n} = 0$$

The equilibrium catalytic wall (ECW) conditions are specified by

$$C_i = C_{i_{eq}} (T_w)$$

In the present work the surface temperatures were sufficiently low that the ECW condition could be approximated by a fully catalytic surface (FCW) condition specified by

$$C_{O_2} = 0.23456 \text{ and } C_{N_2} = 0.76544$$

and the concentration of other species zero.

The shock-boundary condition with slip are the modified Rankine-Hugoniot equations used by Davis.[1] The angle between the freestream velocity vector and a vector tangent to the shock surface and in the plane formed by the normal vector and the freestream velocity vector is denoted by σ. The derivation of σ is given in Murray and Lewis.[5,6] The equations for the conditions behind the shock are given in Appendix B.

3.3 THERMODYNAMIC AND TRANSPORT PROPERTIES

The specific heat, Cp, and static enthalpy, h, are required for each of the species considered and for the gas mixture. Also required are the viscosity, μ, and the thermal conductivity, k. Since the multi-component gas mixture is considered to be a mixture of thermally perfect gases, the thermodynamic and transport properties for each species were calculated using the local temperature. The properties for the gas mixture were then determined in terms of the individual species properties. In this section all expressions are presented in terms of dimensional quantities, and the superscript star is not used to denote dimensional quantities.

The enthalpy and specific heat data of the species were obtained from the thermodynamic data tabulated by Browne.[17-19] A second-order Lagrangian interpolation was used to obtain the values of $\hat{H}_i$ and $\hat{Cp}_i$ from the tables. The species enthalpy and specific heat were then obtained from the expressions

$$h_i = T \hat{H}_i + \Delta h_i^F$$

and

$$Cp_i = \hat{Cp}_i$$

where Δh_i^F is the heat of formation of species i.

The viscosity of each of the individual species was calculated from the curve-fit relation

$$\mu_i = \exp(C_i)\, T_k^{(A_i \ln T_k + B_i)}$$

where A_i, B_i and C_i are the curve-fit constants for each species from Blottner[20] and Yos[21] and T_k is the local temperature in deg. Kelvin. The curve fit coefficients for the species are given in Table 2.

The thermal conductivity of the individual species was calculated from the Eucken semi-empirical formula using the species viscosity and specific heat by the expression

$$k_i = \frac{\mu_i R}{M_i}\left(\frac{Cp_i M_i}{R} + \frac{5}{4}\right)$$

After the viscosity and thermal conductivity of the individual species were calculated, the viscosity and thermal conductivity of the mixture were calculated using Wilke's semi-empirical relations;

$$\mu = \sum_{i=1}^{NS} \left(\frac{X_i \mu_i}{\sum_{j=1}^{NS} X_i \Phi_{ij}} \right)$$

$$k = \sum_{i=1}^{NS} \left(\frac{X_i \, k_i}{\sum_{j=1}^{NS} X_i \Phi_{ij}} \right)$$

where $X_i = C_i \bar{M}/M_i$

and

$$\Phi_{ij} = \left[1 + \left(\frac{\mu_i}{\mu_j} \right)^{1/2} \left(\frac{M_j}{M_i} \right)^{1/4} \right]^2 \left[\sqrt{8} \left(1 + \frac{M_i}{M_j} \right)^{1/2} \right]^{-1}$$

In the present work, the diffusion model is limited to binary diffusion with the binary diffusion coefficients specified by the Lewis number from

$$Le = \rho \, Cp \, Di/k$$

3.4 CHEMICAL REACTION MODEL

In the present study, it is assumed that the fluid medium is a mixture of reacting species and the chemical reactions proceed at a finite rate. The production terms occurring in the energy equation and the species conservation equations

are obtained from the various chemical reactions among the individual species. For a multi-component gas with NS distinct chemical species and NR simultaneous chemical reactions, the chemical reaction equations are written in the general stoichiometric form

$$\sum_{i=1}^{NJ} \alpha_{ri} X_i \underset{k_{br}}{\overset{k_{fr}}{\rightleftharpoons}} \sum_{i=1}^{NJ} \beta_{ri} X_i$$

where r = 1, 2, ... NR and NJ is equal to the sum of the species and the catalytic third bodies. The quantities X_i represent the chemical species and the catalytic third bodies, and the α_{ri} and β_{ri} are the stoichiometric coefficients for reactants and products. The rates at which the forward and backward reactions occur are specified by the forward and backward rate constants which are given by the equations

$$k_{f_r} = T_k^{C2_r} \exp\left(CO_r - C1_r/T_k\right)$$

and

$$k_{b_r} = T_k^{D2_r} \exp\left(DO_r - D1_r/T_k\right)$$

where T_k is the temperature in deg. Kelvin. The constants CO_r, $C1_r$, $C2_r$, DO_r, $D1_r$ and $D2_r$ depend in part on the specific reaction equations chosen. In the present work the reaction-rate constants were taken from Blottner.[11,20]

It is desirable to rewrite the expression for the rate of production terms so that the species concentrations appear as one of the unknowns. When rewritten in this way, the rate of production terms are given by the expression

$$\frac{\dot{w}_i}{\rho} = \dot{w}_i^0 - \dot{w}_i^1 C_i$$

where

$$\dot{w}_i^0 = M_i \sum_{r=1}^{NR} (\Gamma_{ri}^+ L_{f_r} + \Gamma_{ri}^- L_{b_r})$$

$$\dot{w}_i^1 = \sum_{r=1}^{NR} [\Gamma_{ri}^+ (L_{b_r}/\gamma_i) + \Gamma_{ri}^- (L_{f_r}/\gamma_i)]$$

$$\Gamma_{ri}^+ = \begin{cases} (\beta_{ri} - \alpha_{ri}) & \text{if } (\beta_{ri} - \alpha_{ri}) > 0 \\ 0 & \text{if } (\beta_{ri} - \alpha_{ri}) \leq 0 \end{cases}$$

$$\Gamma_{ri}^- = \begin{cases} 0 & \text{if } (\beta_{ri} - \alpha_{ri}) \geq 0 \\ -(\beta_{ri} - \alpha_{ri}) & \text{if } (\beta_{ri} - \alpha_{ri}) < 0 \end{cases}$$

$$L_{f_r} = k_{fr} \exp^{-\alpha_r} \prod_{j=1}^{NJ} (\gamma_j)^{\alpha_{rj}}$$

$$L_{b_r} = k_{b_r} \exp^{-\beta_r} \prod_{j=1}^{NJ} (\gamma_j)^{\beta_{rj}}$$

$$\alpha_r = \sum_{j=1}^{NJ} \alpha_{rj} - 1$$

$$\beta_r = \sum_{j=1}^{NJ} \beta_{rj} - 1$$

$$\gamma_j = \frac{C_j}{M_j} \quad j = 1, 2, \ldots NS$$

The energy equation requires the rate of production terms be rewritten with the temperature appearing as an unknown. That form for the rate of production term was a function of the derivative of $\dot{w}_i/\rho$ with respect to T. With temperature in deg. Kelvin, T_k, the expression for the derivative is

$$\frac{\partial}{\partial T_k}\left(\frac{\dot{w}_i}{\rho}\right) = \frac{M_i}{T_k} \sum_{r=1}^{NR} (\beta_{ri} - \alpha_{ri}) \left[(C2_r + C1_r/T_k - \alpha_r) L_{f_r}\right.$$

$$\left. - (D2_r + D1_r/T_k - \beta_r) L_{b_r}\right]$$

The number of equations to be included in the chemical reaction model depends on the particular problem being considered. For most reentry applications, the temperature in the shock layer is such that a seven species reaction model

with a single ionizing species represents the the actual system reasonably well. The seven species considered are O, O2, N, N2, NO, NO+ and e-. For high energy flows encountered during AOTV applications the temperatures in the shock layer reach as high as 15,000 K and the ionization of atoms and molecules of oxygen and nitrogen have to be considered and an eleven species model consisting of O, O2, N, N2, NO, NO+, O+, O2+, N+, N2+ and e- represents the reactions in the flowfield more accurately.

In this study, seven species and eleven species chemical reaction models were considered for comparison purposes. The seven species model has been used by many investigators and many sources of reaction rate data were available. Hence a seven-reaction rate data from Blottner[11,20] and a twelve-reaction rate data from Kang and Dunn[22] were used in the computations. The seven species models of Blottner and Kang and Dunn are essentially the same except for the fact that Blottner reduced the number of reactions by combining many reactions and modifying the third body matrix to represent the complete system. Most of the computations were performed using Blottner's model, since it is more recent than that of Kang and Dunn. The reactions and reaction rate data from Blottner are given in Table 3 and those from Kang and Dunn are given in Table 4. The reaction rate data for the eleven

species model were obtained from Kang and Dunn and are given in Table 5. They considered 26 reactions to represent the chemical model. It should be noted that the reaction rate data for seven species model from Kang and Dunn is a subset of their reaction rate data for eleven species model. Hence these reaction rate data were used to compare the results from seven species and eleven species models.

3.5 SOLUTION PROCEDURE

The equations are written in the standard form

$$A_0 \frac{\partial^2 W}{\partial \eta^2} + A_1 \frac{\partial W}{\partial \eta} + A_2 W + A_3 + A_4 \frac{\partial W}{\partial \xi} + A_5 \frac{\partial W}{\partial \zeta} = 0$$

and are solved using an efficient finite-difference scheme. The continuity and normal momentum equations are solved by a similar method but they are coupled together. The development of the coupling scheme is given in Ref. 5. The shock stand-off distance is evaluated by integrating the continuity equation.

The solution begins over the spherically blunted nose by obtaining an axisymmetric solution in the wind-fixed coordinate system. The axisymmetric solution is rotated into the body-fixed coordinates and is used as the initial profile for the three-dimensional solution. The three-dimensional

solution begins in the windward plane and marches around the body obtaining a converged solution at each ζ-step. After completing a sweep in ζ, the procedure then steps downstream in ξ and begins the next ζ-sweep. At each point the equations are solved in the following order: (i) species, (ii) ζ-momentum, (iii) energy, (iv) ξ-momentum, (v) integration of continuity for shock stand-off distance and (vi) the coupled continuity and normal momentum equations.

The shock-layer equations depend on $\frac{\partial n_{sh}}{\partial \xi}$ and $\frac{\partial v}{\partial \xi}$ which introduce an elliptic effect into the equations. In the present scheme $\frac{\partial n_{sh}}{\partial \xi}$ is obtained from an inviscid solution, the values of $\frac{\partial v}{\partial \xi}$ are calculated from a backward difference, and the solution is globally iterated until convergence.

Since this code uses a body-oriented orthogonal coordinate system, the geometrical discontinuities have to be treated separately. The forecone is treated as a sphere-cone, and the aftcone is treated separately with the initial data-plane profiles obtained from the forecone flowfield. For expansion corners, the solution procedure is marched on an extension of the upstream geometry past the discontinuity for a streamwise length of 0.6 nose radii. Then the profiles at these two stations are interpolated to obtain the initial data-plane profiles for the aftcone. The flow velocities are

rotated through the expansion angle. For the compression corner, the solution procedure is marched up to the discontinuity. The profiles at the last two stations on the forecone are used to obtain the initial data-plane profiles for the aftcone.

For the bent biconic the aftcone axis is bent with respect to the forecone axis, and the treatment is slightly different. Initially the discontinuity is treated as a straight biconic, and the initial data-plane profiles for the aftcone are obtained by the procedure used for the expansion corners. Subsequently the velocity components are rotated through the bend angle such that they conform to the aftcone coordinate system. The transformation matrices are given in Appendix C.

The forces and moments for the bent biconic are computed differently than those for straight multiconics. The integration of surface pressure and skin friction over the forecone and the aftcone are performed separately. For the forecone the nose tip is used as the reference point whereas, for the aftcone the point of intersection of the two axes is taken as the reference point. Once the forces and moments for the two cones are obtained, the resultant forces and moments for the complete geometry are obtained by transforming

the forecone forces to the aftcone coordinate system and then adding to the aftcone forces. The details of computation of force and moments for bent biconics are given in Appendix D. In this case the center-of-pressure location is given with reference to the base of the body rather than the nose tip.

Chapter IV

RESULTS AND DISCUSSION

The results for the test cases are presented in five sections. The computations by the new method are verified by comparing the results with those from an axisymmetric code VSL7S[3-4] and are presented in section one. The surface-measurable quantities for multiconics and bent biconics computed using the seven species model are presented in section two. These results are compared with those from other inviscid and viscous codes. The surface-measurable quantities for case 3, computed using the seven and eleven species models, are compared in the same section. In section three the shock-layer profiles at a streamwise location of s/Rn = 8.8 on the cone for case 1 computed by both seven and eleven species models are presented. The electron number density at this location computed by the present method is compared with flight data and those computed by Kang and Dunn using an integral method. Section four discusses the aerodynamic force and moment coefficients for the multiconics and bent biconics. In the last section, the computing time required for all computations and the core requirements for the different codes are presented.

4.1 VALIDATION OF VSLNEQ

Figures 5 - 10 show the computational results for case 1a at zero angle-of-attack from the axisymmetric code, VSL7S and the new three-dimensional code, VSLNEQ. The computations were performed for the no-shock-slip and no-wall-slip conditions, and the wall is assumed to be fully catalytic. Figure 5 shows the shock stand-off distance predicted by VSL7S and VSLNEQ. These results are output from the second global iteration. On the sphere, the predictions by both codes are in excellent agreement whereas, on the cone, the shock stand-off distance predicted by VSLNEQ is higher. The maximum difference of 20 % is observed at the end of the body. The difference in shock stand-off distance is believed to be due to the improved differencing schemes used in the present code. In VSL7S, a centered differencing scheme was used, whereas a two point backward differencing scheme was used in VSLNEQ. The earlier code VSL7S, had difficulties in obtaining a smooth shock shape for some cases and this can be seen in the shock slope distribution. (Fig.6) The shock slope distributions predicted by the two codes are in good agreement.

Figures 7-9 show the surface-measurable quantities for case 1a at zero deg. angle-of-attack. These results are

output from the second global iteration. Fig. 7 shows the surface heat-transfer distributions predicted by both codes, and the results are in good agreement. The surface pressure predictions by both codes are in excellent agreement (Fig. 8). The streamwise skin-friction distributions are shown in Fig. 9 and the agreement is excellent. Due to lack of any experimental results these results could not be further verified.

Figure 10 shows the electron concentration profile at s/Rn = 8.8 for various boundary conditions and at the two altitudes under consideration. Computations for both shock slip and no-shock slip are made, and the results are presented. All the computations are made with no wall slip and for a fully catalytic wall. The results from the two codes are within 15% of each other for all the cases considered. The measurements by a fixed bias probe from RAM C flights are presented for comparison. RAM C flights were part of a program conducted by NASA Langley Research Center for studying flowfield electron concentrations under reentry conditions. From the figure the effects of shock slip on the production of electrons can be obtained. At 83.82 km (275kft) the low density effects are more predominant, and the computation with no-shock slip gives the electron concentration about two orders lower than the experiment. With

shock slip the results are closer to the experimental results. Still both codes underpredict the electron concentration at 83.82 km (275kft) by about a factor of four. These computations are made with no-wall slip, and at this altitude the low density effects are important, thus making it necessary to include the wall-slip effects into the computations. It is felt that the wall-slip effects will change the temperature profile considerably and this in turn will change the electron concentration. At 70.104 km (230kft) the shock-slip effects are negligible. Both codes overpredict the electron concentration at 70.104 km (230kft).

With these comparisons, it can be concluded that the new method is validated to the level of confidence of the earlier method.

4.2 SURFACE MEASURABLE QUANTITIES

The results from the seven-species nonequilibrium code have been compared with those from other inviscid and viscous codes. NOL3D[13,14] is used to obtain the inviscid shock shapes and the inviscid surface pressure. A viscous shock-layer code, VSLET[8] has been modified to analyze the multiconics in perfect gas and equilibrium air flow, and the results are presented for comparison. Some sample results

recieved from Gnoffo[12] have been used to compare the viscous shock-layer results with those from a parabolized Navier-Stokes method. The following discussion is presented in two parts. The first part deals with straight multiconics, whereas, the second part discusses the results for the bent biconic.

4.2.1 Straight multiconics

Figures 11 to 18 show the surface pressure and surface heat-transfer distributions for the 9/4 biconic (case 2) and a sphere-cone-cylinder-flare (case 3) for zero and nonzero angles-of-attack. Figure 11 shows the surface pressure distribution for the 9/4 biconic at five deg. angle-of-attack for windward and lee planes. The inviscid pressure predicted by NOL3D is presented for comparison. The perfect gas and nonequilibrium pressure predictions are in good agreement. Figure 12 shows the surface heat-transfer distribution for 5 deg. angle-of-attack. The nonequilibrium heat transfer is higher by about 15% for the entire length of the body. The nonequilibrium computations are performed for fully catalytic wall conditions. Since the inverse Reynolds number parameter is quite high for this case, the flow is closer to frozen flow and hence the diffusion heat transfer is not very high. Figure 13 shows the streamwise skin-fric-

tion distribution for case 2 at five deg. angle-of-attack. The skin friction for the nonequilibrium, fully catalytic wall is higher than that for for the perfect gas throughout the length of the body for windward and lee planes.

Figure 14 shows the circumferential surface pressure distribution at two axial locations for case 2 at five deg. angle of attack. The first point at z/Rn = 10 is on the forecone whereas the second location is near the base of the body on the aftcone. The nonequilibrium and perfect gas pressures are in good agreement at these locations. Figure 15 shows the circumferential skin friction distribution at these locations for case 2. The maximum circumferential skin-friction occurs at about ϕ = 70 deg. and the nonequilibrium skin friction is higher than that for the perfect gas.

Figure 16 shows the surface pressure distribution for the sphere-cone-cylinder-flare at zero angle-of-attack. The nonequilibrium pressure on the flare is higher than the perfect gas pressure by about 20%. The surface-pressure distribution computed using the eleven species model compares very well with that computed using the seven species model. Figure 17 shows the surface heat-transfer distribution for sphere-cone-cylinder-flare at zero angle-of-attack. The diffusion heat-transfer rate on the flare is much higher

than that on the rest of the body. The dissociation of molecules and ionization of molecules and atoms in the shock layer depend on the temperature and pressure in the shock layer, and the concentrations of dissociated and ionized species increase with pressure. The higher pressure on the flare increases the concentration of these species which in turn increases the diffusion toward the wall. This causes a higher diffusion heat transfer on the flare. The heat-transfer distribution computed by the eleven species model is also plotted for comparison and the agreement is good. Figure 18 shows the streamwise skin-friction distribution for this case. The skin friction computed using the eleven species model agrees well with that from the seven species code. Once again the influence of the flare on the surface-measurable quantities is seen.

4.2.2 Bent biconic

Figures 19, 20, and 21 show the surface pressure distribution for α = 0, 10, and 20 deg. for various ϕ-planes. The angle-of-attack for the bent biconic is measured from the aftcone axis. In general, the surface pressure predictions by various codes are in good agreement on the windward side and 90 deg. plane, whereas, the predictions for the leeward side differ for most cases. On the aftcone the inviscid code

shows a considerable overexpansion on the windward side, whereas the results from the viscous codes are in good agreement. The viscous shock-layer method is parabolic in the crossflow direction as well as the streamwise marching direction, and hence the VSL method cannot treat crossflow separation. The VSL code has been written in such a way that the separated flowfield is not analyzed.

Figures 22, 23 and 24 show the surface heat-transfer distribution for α = 0, 10, and 20 deg. for various ϕ-planes. The nonequilibrium calculations have been performed using fully catalytic wall boundary conditions. The nonequilibrium heat transfer is higher in general for all the cases considered. For α = 0 the equlibrium heat transfer also is plotted for comparison. For this computation, the equilibrium air properties were obtained from equilibrium tables using a Table-Look-Up procedure. For α = 0 deg., the equilibrium heat transfer on the windward plane initially increases and then decreases to a value closer to the predictions by other cases. This behaviour cannot be explained at present with the available data. The equlibrium-air heat transfer is higher for most cases.

Figures 25, 26 and 27 show streamwise skin-friction distributions for case 4 at α = 0, 10, 20 deg. for various ϕ

planes. The trend is similar to that observed in the heat-transfer distribution.

4.3 SHOCK-LAYER PROFILES

Figures 28 to 31 show the shock-layer profiles for case 1 at a streamwise location of 8.8 nose radii. Figure 28 shows the electron number density for case 1 at s/Rn = 8.8 computed by the present method using both seven and eleven species chemical reaction models. The results obtained by Kang and Dunn using an integral method and experimental data from RAM C flights are presented for comparison. The computations by the present method were performed for a fully catalytic wall with no-wall slip. Without shock slip, the present method with the seven species model considerably underpredicted the electron number density. The results from the present method using the eleven species model were higher than those from the seven species model. With shock slip both models predicted higher electron density. Without shock slip the species concentrations behind the shock were the same as in the freestream and thus the concentrations of both NO+ and electrons were zero. With shock slip, however, a finite concentration of NO+ and thus e- was permitted behind the shock and diffusion carried the ions to the shock zone. While the electron density at the shock was quite low with shock slip,

the nonzero concentration of NO+ behind the shock raised the electron density profile. Also with shock slip both models predicted a thicker viscous shock layer and higher static temperature (see Fig. 29.) The increased temperature increases the ionization and hence leads to higher electron density.

The eleven species model considered five ionizing species and each of these species contribute to the electron density. Even though the concentration of NO+ predicted by the seven species model was higher than that predicted by the eleven species model, the concentration of O2+ is higher than that of NO+ at these conditions (Fig. 30). The concentration of O+ and N2+ are an order or more lower than that of NO+ and O2+ and hence have less influence on the electron density. The concentration on N+ was in traces, and this is explainable by the temperature levels attained in the shock layer. The maximum temperature in the shock layer was about 10,000 R, and at these conditions the ionization of atoms is small. Also by looking at the concentrations of the dissociated species (Fig. 31) it can be seen that there was little dissociation and hence fewer atoms were present to be ionized. This also explains the higher levels of O2+ and N2+. The predictions of dissociated atoms and the temperature profiles by both seven species and eleven species models are in good agreement.

Comparing the electron density predicted by the present method with flight data shows that the seven species model underpredicts the electron density, whereas the eleven species model overpredicts the flight data. It should be noted that at this altitude of 88.32 m (275 kft) the low density effects are important and so the slip effects should be included. These computations are made assuming shock slip and no-wall slip. The effect of wall-slip should be considered before any conclusions on the accuracy of these models are stated. The low concentrations of N+, O+ and N2+ show that the ionization is low for this case, and a seven species model should be sufficient to represent the reactions occurring at these conditions provided the wall-slip effects are considered.

Comparing the electron density predicted by the present method with that predicted by Kang and Dunn there was considerable difference in the magnitude and the distribution of electron density in the shock layer. Although the electron density predicted by the eleven species model of Kang and Dunn is closer to the flight data in the shock layer, the upward swing near the shock and the peak at the shock cannot be explained. The present method predicted the peak of the electron density profile correctly in the shock layer but not at the shock. Since the maximum temperature in the

shock layer is near the shock and not at the shock, the prediction of peak electron density at the shock by Kang and Dunn cannot be explained.

The main emphasis of the present work was on predicting the hypersonic viscous flowfield over complex bodies, with electron concentration profiles only a part of the flowfield prediction. Since the electron concentration profiles are subject to changes in reaction-rate constants as well as changes in temperature profile, mean flowfield quantities such as heat-transfer and skin-friction distributions would be a more reliable method of verifying the new method. From the previous section it can be seen that the surface-measurable quantities predicted by the two models are in good agreement.

4.4 AERODYNAMIC FORCES AND MOMENTS

Table 6 shows the aerodynamic force and moment coefficients for the straight multiconics. For case 2, the center-of-pressure location predicted by the viscous codes is about 7% to 10% downstream of that predicted by the inviscid code. The forces and moments for the nonequilibrium case are higher than those for the perfect gas case.

Figures 32 and 33 show the variation of normal force and pitching moment coefficients with angle-of-attack. The normal force coefficient for the nonequilibrium case is lower than that for the perfect gas case. It should be noted that the pitching moment is measured from the base of the body and not from nose tip. Table 7 shows the force and moment coefficients for this case in a tabular form.

4.5 COMPUTING TIME

The computing times required for analyzing the nonequilibrium flowfield for case 1 using VSL7S and VSLNEQ are compared with those required for a perfect gas in Table 8. The nonequilibrium calculations require about an order of magnitude more computing time than the perfect gas. In general the computing time is more for the shock-slip cases. At the lower altitude the flow is closer to equilibrium and hence, the nonequilibrium code requires more time for the solution. However, it should be noted that these three-dimensional, finite-rate, chemically reacting, laminar, hypersonic, viscous flowfield solutions have been obtained in reasonable computing times on general purpose computers (IBM 370/3032 or 3081). The new code, VSLNEQ, with the simple sphere-cone capability has a core requirement of 255 kbytes, whereas the axisymmetric code VSL7S required about 265 kbytes. This is

mainly due to the fact that VSL7S uses a centered-differencing scheme which requires more storage, whereas the VSLNEQ uses a 2 point backward-differencing scheme.

Table 9 shows the computing time for the various test cases considered. The computing time is based on IBM 370/3081, H=OPT2 compiler. The zero angle-of-attack case for each case has been taken as a reference, and the time ratios for each test case are also presented. The nonequilibrium cases took about 4 to 5 times longer than the perfect gas cases. The equilibrium case used a Table-Look-Up procedure for obtaining the equilibrium air properties and hence took about 75% more time than the nonequilibrium case. The seven species nonequilibrium code capable of solving multiconics and bent biconics has a core requirement of 635 kbytes, whereas the perfect gas and equilibrium air code needs 540 kbytes.

The eleven species nonequilibrium code capable of analyzing multiconics bent biconics needs about 690 kbytes to load. The computing time for the eleven species nonequilibrium code is about 2.8 times that of the seven species nonequilibrium code. This time estimate is based on a convergence criterion of 1% of relative difference on all the flow variables and species concentrations. This condition is too

stringent for the eleven species model where the concentrations of some of the species become too small. For some cases, this convergence criterion makes it impossible to obtain a converged solution. Hence the convergence criterion for the eleven species model is modified to 1% of relative difference on all flow variables and those species with concentrations more than 1%. Once these variables are converged, the rest of the variables are assumed to be converged. With this modification the computing time for the eleven species nonequilibrium code is comparable to that for the seven species nonequilibrium code.

Chapter V

CONCLUDING REMARKS

From the results for case 1 and 2 it is seen that a viscous shock-layer method for solving the three-dimensional nonequilibrium flow over axisymmetric, blunted sphere-cones within reasonable computing time is developed. The new code has been verified by comparing the surface-measurable quantities and shock-layer profiles for case 1 at zero angle-of-attack with those from an earlier axisymmetric code.

The computational results for three-dimensional nonequilibrium flowfields over straight and bent multiconics have been compared with perfect gas and equilibrium air results. The surface-pressure distributions over straight and bent multiconics agree well with those predicted by other viscous codes. The diffusion heat transfer is about 15% for most cases considered. The aerodynamic force and moment coefficients at the base of the body for the straight multiconics and the bent biconic have been computed. In conclusion, a method for analyzing the three-dimensional nonequilibrium flow over straight and bent biconics in reasonable computing time is demonstrated.

The surface-measurable quantities computed using the eleven species model agree very well with those computed using the seven species model for reentry flight conditions. However the eleven species model with shock slip overpredicts the electron number density, whereas the seven species model with shock slip under predicts the electron density.

REFERENCES

1. Davis, R. T.: "Numerical Solution of the Hypersonic Viscous Shock-Layer Equations," AIAA J., May 1970, pp. 843-851.

2. Srivastava, B. N., Werle, M. J. and Davis, R. T.: "Stagnation Region Solutions of the Full Viscous Shock-Layer Equations," AIAA J., February 1976, pp. 274-276.

3. Miner, E. W. and Lewis, C. H.: "Hypersonic Ionizing Air Viscous Shock-Layer Flows over Nonanalytic Blunt Bodies," NASA CR-2550, May 1975. Also AIAA J., January 1976, pp. 64-69.

4. Miner, E. W. and Lewis, C. H.: "Computer User's Guide for a Chemically Reacting Viscous Shock-Layer Program," NASA CR-2551, May 1975.

5. Murray, A. L. and Lewis, C. H.: "Three Dimensional Fully Viscous Shock-Layer Flows over Sphere-cones at High Altitudes and High Angles of Attack," VPI-AERO-078, March 1975.

6. Murray, A. L. and Lewis, C. H: "Hypersonic Three-Dimensional Viscous Shock- Layer Flow over Blunt Bodies," AIAA J., Vol. 16, No. 12, pp.1279-1286, December 1978.

7. Szema, K. Y. and Lewis, C. H.: "Three-Dimensional Hypersonic Laminar, Transitional and/or Turbulent Shock-Layer Flows," Journal of Spacecrafts and Rockets, vol., 19 Jan. 1982, pp.88-91. July 1980.

8. Thareja, R. R., Szema, K. Y. and Lewis, C. H.: "Effects of Chemical Equilibrium on Three-Dimensional Viscous Shock-Layer Analysis of Hypersonic Laminar or Turbulent Flows," AIAA Paper No. 82-0305, January 1982.

9. Miller, C. G. and Gnoffo, P. A.: "Pressure Distributions and Shock Shapes for 12.84/7 On-Axis and Bent-Nose Biconics in Air at Mach 6" NASA TM-83222, Dec. 1981.

10. Miller, C. G., and Gnoffo, P. A.: "An Experimental Investigation of Hypersonic Flow over Biconics at Incidence and Comparison to Prediction AIAA Paper No.

82-1382. AIAA 9th Atmospheric Flight Mechanics Conference. San Diego, CA, August 9-11, 1982

11. Blottner, F. G. "Nonequilibrium Laminar Boundary Layer Flow of Ionized Air." Report no. R64SD56, Space Sciences Laboratory, General Electric. Nov. 1964

12. Gnoffo, P. A. Private communications

13. Solomon, J. M., Ciment, M., Ferguson, R. E., Bell, J. B. and Wardlaw, Jr., A. B.: A program for computing Steady Inviscid Three-Dimensional Supersonic Flow on reentry Vehicles, Vol. I, Analysis and Programming," Report No. NSWC/WOL/TR 77-28, February 1977.

14. Solomon, J. M., Ciment, M., Ferguson, R. E., Bell, J. B. and Wardlaw, Jr., A. B.: A program for computing Steady Inviscid Three-Dimensional Supersonic Flow on reentry Vehicles, Vol. II, User's Manual," NSWC/WOL/TR 77-28, February 1977.

15. Bird, R. B., Stewart, W. E. and Lightfoot, E. N., Transport Phenomena, John Wiley and Sons, Inc., 1960.

16. Williams, F., Combustion Theory, Addison Wesley Book Co., Inc., 1965.

17. Browne, W. G.: "Thermodynamic Properties of Some Atoms and Atomic Ions," MSD Engineering Physics TM2, General Electric Co., Philadelphia, Pa.

18. Browne, W. G.: "Thermodynamic Properties of Some Diatomic and Linear Polyatomic Molecules," MSD Engineering Physics TM3, General Electric Co., Philadelphia, Pa.

19. Browne, W. G.: "Thermodynamic Properties of Some Diatoms and Diatomic Ions at High Temperature," MSD Advanced Aerospace Physics TM8, General Electric Co., Philadelphia, Pa., May 1962.

20. Blottner, F. G., Johnson, Margaret and Ellis, Molly: "Chemically Reacting Viscous Flow Program for Multi-Component Gas Mixtures," Sandia Laboratories Report SC-RR-70-754, December 1971.

21. Yos, J. M. "Revised Transport Properties for High Temperature Air and its Components. Technical release, Nov. 28, 1967, Space Systems Division, Avco Corp., Wilmington, MASS.

22. Kang, S. W., Dunn, M. G.: Theoretical and Experimental Studies of Reentry Plasmas. NASA CR-2232, April 1973.

Appendix A

GOVERNING EQUATIONS

The viscous shock-layer equations are derived from the Navier-Stokes equations for a reacting mixture, as given by Bird, Stewart and Lightfoot[15] and Williams.[16] The Navier-Stokes equations in dimensional variables are given in vector form as follows.

Continuity equation: $$\frac{\partial \rho}{\partial t} + \nabla \cdot \rho \bar{V} = 0$$

Momentum equation: $$\rho \frac{D\bar{V}}{Dt} = -\nabla p - \nabla \cdot \bar{\bar{\tau}} + \rho \bar{g}$$

Energy equation: $$\rho \frac{Dh}{Dt} = -\nabla \cdot \bar{q} + \rho(\bar{V} \cdot \bar{g}) - \bar{\bar{\tau}} : \nabla \bar{V} + \frac{DP}{Dt} - \sum_{i=1}^{NS} C_{p_i} J_i \frac{\partial T}{\partial y} - \sum_{i=1}^{NS} h_i \dot{w}_i$$

Species equation: $$\rho \frac{DC_i}{Dt} = \nabla \cdot J_i + \dot{w}_i$$

The following assumptions and steps are involved in derriving the viscous shock-layer equations. (see Ref. 5 for details)

1. Assume steady flow and no body forces
2. Write equations in surface-normal coordinates.
3. Nondimensionalize by reference variables
4. Assuming v and n are of the order of ε, neglect terms of higher order than ε
5. Normalize the shock-layer equations by quantities behind the bow shock. The velocity components v and w, the temperature T, and the species concentration C_i are not normalized to avoid division by small numbers.

Among the resulting set of conservation equations, the continuity and normal momentum equations are coupled together and solved simultaneously.

Continuity

$$\frac{\partial}{\partial\xi}\left(\rho_{sh}u_{sh}\bar{\rho}\bar{u}h_3\right) - \frac{n}{n_{sh}}\frac{\partial n_{sh}}{\partial\xi}\frac{\partial}{\partial n}\left(\rho_{sh}u_{sh}\bar{\rho}\bar{u}h_3\right) + \frac{1}{n_{sh}}\frac{\partial}{\partial n}\left(h_1h_3\rho_{sh}\bar{\rho}\bar{v}\right)$$

$$+ \frac{\partial}{\partial\zeta}\left(\rho_{sh}\bar{\rho}\bar{w}h_1\right) - \frac{n}{n_{sh}}\frac{\partial n_{sh}}{\partial\zeta}\frac{\partial}{\partial n}\left(\rho_{sh}\bar{\rho}\bar{w}h_1\right) = 0$$

n-Momentum

$$\frac{\rho_{sh}u_{sh}\bar{\rho}\bar{u}}{h_1}\frac{\partial v}{\partial\xi} + \frac{\rho_{sh}\bar{\rho}\bar{v}}{n_{sh}}\frac{\partial v}{\partial n} - \frac{\rho_{sh}u_{sh}\bar{\rho}\bar{u}n}{h_1n_{sh}}\frac{\partial n_{sh}}{\partial\xi}\frac{\partial v}{\partial n} + \frac{\rho_{sh}\bar{\rho}\bar{w}}{n_3}\frac{\partial v}{\partial\zeta}$$

$$- \frac{\rho_{sh}\bar{\rho}\bar{w}n}{h_3n_{sh}}\frac{\partial n_{sh}}{\partial\zeta}\frac{\partial v}{\partial n} - \frac{\rho_{sh}u_{sh}^2\bar{\rho}\bar{u}^2}{h_1n_{sh}}\frac{\partial h_1}{\partial n} - \frac{\rho_{sh}\bar{\rho}\bar{w}^2}{h_3n_{sh}}\frac{\partial h_3}{\partial n} + \frac{\rho_{sh}}{n_{sh}}\frac{\partial\bar{p}}{\partial n} = 0$$

The remaining equations are parabolic and may be expressed in the standard form

$$A_0 \frac{\partial^2 W}{\partial \eta^2} + A_1 \frac{\partial W}{\partial \eta} + A_2 W + A_3 + A_4 \frac{\partial W}{\partial \xi} + A_5 \frac{\partial W}{\partial \zeta} = 0$$

where W is the dependent variable u, w or h.

<u>ξ-Momentum</u>

$$A_0 = -\frac{\varepsilon^2 \mu_{sh} u_{sh} \bar{\mu}}{n_{sh}^2}$$

$$A_1 = -\frac{\varepsilon^2 \mu_{sh} u_{sh}}{n_{sh}^2} \frac{\partial \bar{\mu}}{\partial \eta} + \frac{\varepsilon^2 \mu_{sh} u_{sh} \bar{\mu}}{n_{sh}^2 h_1} \frac{\partial h_1}{\partial \eta} - \frac{\rho_{sh} u_{sh}^2 \eta}{h_1 n_{sh}} \frac{\partial n_{sh}}{\partial \xi} \bar{\rho}\bar{u}$$

$$+ \frac{\rho_{sh} u_{sh} \bar{\rho} v}{n_{sh}} - \frac{\rho_{sh} u_{sh} \eta \bar{\rho} w}{h_3 n_{sh}} \frac{\partial n_{sh}}{\partial \zeta} - \frac{\varepsilon^2 \mu_{sh} \bar{\mu} u_{sh}}{n_{sh}^2} \left(\frac{2}{h_1} \frac{\partial h_1}{\partial \eta} + \frac{1}{h_3} \frac{\partial h_3}{\partial \eta} \right)$$

$$A_2 = \frac{\rho_{sh} u_{sh} \bar{\rho}\bar{u}}{h_1} \frac{\partial u_{sh}}{\partial \xi} + \frac{\rho_{sh} \bar{\rho} w}{h_3} \frac{\partial u_{sh}}{\partial \zeta} + \frac{\rho_{sh} u_{sh}}{h_1 n_{sh}} \frac{\partial h_1}{\partial \eta} \bar{\rho}\bar{u}$$

$$+ \frac{\rho_{sh} u_{sh} \bar{\rho} w}{h_1 h_3} \frac{\partial h_1}{\partial \zeta} - \frac{\rho_{sh} u_{sh} \bar{\rho} w \eta}{h_1 h_3 n_{sh}} \frac{\partial n_{sh}}{\partial \zeta} \frac{\partial h_1}{\partial \eta} + \frac{\varepsilon^2 \mu_{sh} u_{sh}}{n_{sh}^2} \frac{\partial}{\partial \eta} \left(\frac{\bar{\mu}}{h_1} \frac{\partial h_1}{\partial \eta} \right)$$

$$+ \frac{\varepsilon^2 \mu_{sh} u_{sh} \bar{\mu}}{n_{sh}^2 h_1} \left(\frac{2}{h_1} \frac{\partial h_1}{\partial \eta} + \frac{1}{h_3} \frac{\partial h_3}{\partial \eta} \right) \frac{\partial h_1}{\partial \eta}$$

$$A_3 = -\frac{\rho_{sh} \bar{\rho} w^2}{h_1 h_3} \frac{\partial h_3}{\partial \xi} + \frac{\rho_{sh} \eta}{h_1 h_3 n_{sh}} \frac{\partial n_{sh}}{\partial \xi} \bar{\rho} w^2 \frac{\partial h_3}{\partial \eta}$$

$$+ \frac{\bar{p}}{h_1} \frac{\partial p_{sh}}{\partial \xi} + \frac{p_{sh}}{h_1} \frac{\partial \bar{p}}{\partial \xi} - \frac{\rho_{sh} \eta}{h_1 n_{sh}} \frac{\partial n_{sh}}{\partial \xi} \frac{\partial \bar{p}}{\partial \eta}$$

$$A_4 = \frac{\rho_{sh} u_{sh}^2 \bar{\rho}\bar{u}}{h_1} \qquad A_5 = \frac{\rho_{sh} u_{sh} \bar{\rho} w}{h_3}$$

ξ-Momentum

$$A_0 = -\frac{\varepsilon^2 \mu_{sh} \bar{\mu}}{n_{sh}^2}$$

$$A_1 = -\frac{\rho_{sh} u_{sh} \bar{\rho}\bar{u}\eta}{h_1 n_{sh}} \frac{\partial n_{sh}}{\partial \xi} + \frac{\rho_{sh} \bar{\rho} v}{n_{sh}} - \frac{\rho_{sh} \eta \bar{\rho} w}{h_3 n_{sh}} \frac{\partial n_{sh}}{\partial \zeta} - \frac{\varepsilon^2 \mu_{sh}}{n_{sh}^2} \frac{\partial \bar{u}}{\partial \eta} - \frac{\varepsilon^2 \mu_{sh} \bar{\mu}}{n_{sh}^2 h_3} \frac{\partial h_3}{\partial \eta}$$

$$- \frac{\varepsilon^2 \bar{u} \mu_{sh}}{h_1 n_{sh}^2} \frac{\partial h_1}{\partial \eta}$$

$$A_2 = \frac{\rho_{sh} u_{sh} \bar{\rho}\bar{u}}{h_1 h_3} \frac{\partial h_3}{\partial \xi} - \frac{\rho_{sh} u_{sh} \bar{\rho}\bar{u}\eta}{h_1 h_3 n_{sh}} \frac{\partial n_{sh}}{\partial \xi} \frac{\partial h_3}{\partial \eta} + \frac{\rho_{sh} \bar{\rho} v}{h_3 n_{sh}} \frac{\partial h_3}{\partial \eta} + \frac{\varepsilon^2 \mu_{sh} \bar{\mu}}{h_3 n_{sh}^2} \frac{\partial^2 h_3}{\partial \eta^2}$$

$$+ \frac{\varepsilon^2 \mu_{sh} \bar{\mu}}{n_{sh}^2 h_3^2} \left(\frac{\partial h_3}{\partial \eta} \right)^2 + \frac{\varepsilon^2 \mu_{sh}}{h_3 n_{sh}^2} \frac{\partial \bar{u}}{\partial \eta} \frac{\partial h_3}{\partial \eta} + \frac{\varepsilon^2 \mu_{sh} \bar{\mu}}{h_1 h_3 n_{sh}^2} \frac{\partial h_1}{\partial \eta} \frac{\partial h_3}{\partial \eta}$$

$$A_3 = -\frac{\rho_{sh} u_{sh}^2 \bar{\rho}\bar{u}^2}{h_1 h_3} \frac{\partial h_1}{\partial \zeta} + \frac{\rho_{sh} u_{sh}^2 \bar{\rho}\bar{u}^2 \eta}{h_1 h_3 n_{sh}} \frac{\partial n_{sh}}{\partial \zeta} \frac{\partial h_1}{\partial \eta} + \frac{p_{sh}}{h_3} \frac{\partial \bar{p}}{\partial \zeta} + \frac{\bar{p}}{h_3} \frac{\partial p_{sh}}{\partial \zeta}$$

$$- \frac{p_{sh} \eta}{h_3 n_{sh}} \frac{\partial n_{sh}}{\partial \zeta} \frac{\partial \bar{p}}{\partial \eta}$$

$$A_4 = \frac{\rho_{sh} u_{sh} \bar{\rho}\bar{u}}{h_1} \qquad A_5 = \frac{\rho_{sh} \bar{\rho} w}{h_3}$$

Energy

$$A_0 = -\frac{\varepsilon^2 \bar{k} k_{sh}}{n_{sh}^2}$$

$$A_1 = \frac{\bar{\rho}\rho_{sh} v C_p}{n_{sh}} - \frac{\bar{\rho}\rho_{sh} \bar{u} u_{sh} C_p \eta}{h_1 n_{sh}} \left(\frac{\partial n_{sh}}{\partial \xi} \right) - \bar{\rho}\rho_{sh} w C_p \eta \left(\frac{\partial n_{sh}}{\partial \zeta} \right) - \frac{\varepsilon^2 k_{sh}}{n_{sh}^2} \left(\frac{\partial \bar{k}}{\partial \eta} \right)$$

$$- \frac{\varepsilon^2 \bar{k} k_{sh}}{h_3 n_{sh}^2} \frac{\partial h_3}{\partial \eta} - \frac{\varepsilon^2 \bar{k} k_{sh}}{h_1 n_{sh}^2} \left(\frac{\partial h_1}{\partial \eta} \right) + \frac{\varepsilon^2 (\Sigma J_i C_{pi})}{n_{sh}} \quad \text{where } J_i = -\frac{\mu}{Pr} \, Le \, \frac{\partial C_i}{\partial y}$$

$$A_3 = \dot{w}_2$$

$$A_3 = -\frac{\rho_{sh}\bar{u}u_{sh}}{h_1}\frac{\partial\bar{p}}{\partial\xi} - \bar{u}u_{sh}\bar{\rho}\left(\frac{\partial p_{sh}}{\partial\xi}\right) + \rho_{sh}\bar{u}u_{sh}\eta\left(\frac{\partial n_{sh}}{\partial\xi}\right)\left(\frac{\partial\bar{\rho}}{\partial n}\right) - \frac{\rho_{sh}}{n_{sh}}v\left(\frac{\partial\bar{p}}{\partial n}\right)$$

$$- \frac{w}{h_3}\frac{\partial(\bar{\rho}p_{sh})}{\partial\zeta} + \frac{\rho_{sh}w\eta}{h_3 n_{sh}}\left(\frac{\partial n_{sh}}{\partial\zeta}\right)\frac{\partial\bar{\rho}}{\partial n} - \varepsilon^2\bar{u}u_{sh}\left[\frac{u_{sh}}{n_{sh}}\frac{\partial\bar{u}}{\partial n} - \frac{\bar{u}u_{sh}}{h_1 n_{sh}}\left(\frac{\partial h_1}{\partial n}\right)\right]^2$$

$$- \varepsilon^2\bar{u}u_{sh}\left[\frac{\left(\frac{\partial w}{\partial n}\right)}{n_{sh}} - \frac{w\left(\frac{\partial h_3}{\partial n}\right)}{h_3 n_{sh}}\right]^2 + \dot{w}_1$$

$$A_4 = \frac{\bar{\rho}\rho_{sh}\bar{u}u_{sh}C_p}{h_1} \qquad A_5 = \frac{\bar{\rho}\rho_{sh}\bar{w}C_p}{h_3}$$

Species

$$A_0 = \frac{\varepsilon^2}{n_{sh}^2}\frac{\mu_{sh}\bar{\mu}Le}{Pr}$$

$$A_1 = \frac{\varepsilon^2}{n_{sh}^2}\frac{\partial}{\partial n}\left(\frac{\mu_{sh}\bar{\mu}Le}{Pr}\right) + \frac{\varepsilon^2}{n_{sh}}\frac{1}{h_3}\frac{\bar{\mu}u_{sh}Le}{Pr}\frac{\partial h_3}{\partial n} + \frac{\varepsilon^2}{n_{sh}^2}\frac{1}{h_1}\frac{\bar{\mu}u_{sh}Le}{Pr}\frac{\partial h_1}{\partial n}$$

$$+ \frac{\bar{\rho}\rho_{sh}w}{h_3}\frac{\eta}{n_{sh}}\frac{\partial n_{sh}}{\partial\zeta} + \frac{\bar{\rho}\rho_{sh}\bar{u}u_{sh}}{h_1}\frac{\eta}{n_{sh}}\frac{\partial n_{sh}}{\partial\xi} - \frac{\bar{\rho}\rho_{sh}v}{n_{sh}}$$

$$A_2 = -\rho_{sh}\bar{\rho}\dot{w}_i^1 \qquad A_3 = \rho_{sh}\bar{\rho}\dot{w}_i^0$$

$$A_4 = -\frac{\bar{\rho}\rho_{sh}\bar{u}u_{sh}}{h_1} \qquad A_5 = -\frac{\bar{\rho}\rho_{sh}w}{h_3}$$

Appendix B

SHOCK BOUNDARY CONDITIONS

The shock boundary conditions with slip are the modified Rankine-Hugoniot equations used by Davis.[1] The angle between the freestream velocity vector and a tangent to the shock surface and in the plane formed by the normal vector and freestream velocity vector is denoted by σ. The derivation of σ is given in Ref. 5 The equations for the conditions behind the shock are

$$\hat{u}_{sh} = \frac{\cos\sigma}{1 + \frac{\varepsilon^2}{n_{sh}} \frac{\mu_{sh}}{\sin\sigma} \left(\frac{\partial \hat{u}}{\partial \eta}\right)} \tag{B-1}$$

$$T_{sh} = \frac{0.5(\hat{u}_{sh}-\cos\sigma)^2 + 0.5(\sin^2\sigma-\hat{v}_{sh}^2) + \sum_{i=1}^{NS} C_{i_\infty} h_{i_\infty}}{\sum_{i=1}^{NS} C_{i_\infty} \left(\frac{h_{i_{sh}}}{\bar{T}_{sh}}\right) + \frac{\varepsilon^2}{n_{sh}} \frac{k_{sh}}{\sin\sigma} \left(\frac{\partial \bar{T}}{\partial \eta}\right)} \tag{B-2}$$

$$p_{sh} = \frac{p_\infty^*}{\rho_\infty^* u_\infty^{*2}} + \sin\sigma\,(\hat{v}_{sh} + \sin\sigma) \tag{B-3}$$

$$\rho_{sh} = \frac{p_{sh}}{T_{sh} \left(\frac{R}{C_{pref}}\right)} \tag{B-4}$$

$$\hat{v}_{sh} = -\frac{\sin\sigma}{\rho_{sh}} \tag{B-5}$$

$$C_{i_{sh}} = C_{i_\infty} - \varepsilon^2 \left(\frac{\mu Le_i}{Pr}\right)_{sh} \frac{1}{n_{sh}} \frac{\partial C_i}{\partial \eta} \frac{1}{\sin\sigma} \tag{B-6}$$

Appendix C

VELOCITY TRANSFORMATION FOR BENT BICONIC

Initially the geometrical discontinuity for the bent biconic is treated as that for a straight biconic, and the initial data-plane profile for the aftcone is obtained by the procedure used for straight biconic. The initial data-plane velocity components for the straight biconic are u, v and w. These velocities are then transformed to the aftcone coordinate system by the following transformation

$$\begin{bmatrix} u' \\ v' \\ w' \end{bmatrix} = [E]\,[D]\,[C]\,[B]\,[A] \begin{bmatrix} u \\ v \\ w \end{bmatrix}$$

Where $[E] = \begin{bmatrix} \cos\theta_x & \sin\theta_x & 0 \\ -\sin\theta_x & \cos\theta_x & 0 \\ 0 & 0 & 1 \end{bmatrix}$

$$[D] = \begin{bmatrix} 1 & 0 & 0 \\ 0 & \cos\phi' & \sin\phi' \\ 0 & -\sin\phi' & \cos\phi' \end{bmatrix}$$

$$[C] = \begin{bmatrix} \cos\theta_b & 0 & \sin\theta_b \\ 0 & 1 & 0 \\ -\sin\theta_b & 0 & \cos\theta_b \end{bmatrix}$$

$$[B] = \begin{bmatrix} 1 & 0 & 0 \\ 0 & \cos\phi' & -\sin\phi' \\ 0 & \sin\phi' & \cos\phi' \end{bmatrix}$$

$$[A] = \begin{bmatrix} \cos\theta_x & -\sin\theta_x & 0 \\ \sin\theta_x & \cos\theta_x & 0 \\ 0 & 0 & 1 \end{bmatrix}$$

where θ_x = body angle in the streamwise direction.

ϕ' = $\phi - \pi/2$

θ_b = bend angle, ie. the angle between the forecone and aftcone axes.

Appendix D

FORCE AND MOMENT COMPUTATION FOR A BENT BICONIC

The axial and normal forces for the forecone and aftcone are computed separately and are given by

F_{A_1} = Axial force of forecone based on forecone coordinate system

F_{N_1} = Normal force of forecone based on forecone coordinate system

Z_{CP_1} = Center-of-pressure location of forecone measured from nose tip

F_{A_2} = Axial force of aftcone based on aftcone coordinate system

F_{N_2} = Normal force of aftcone based on aftcone coordinate system

Z_{CP_2} = Center-of-pressure location of aftcone measured from the point of intersection of the axes

The axial and normal force on the forecone are then transformed to the aftcone coordinate system. The prime (') indicates the transformed quantities.

$$\begin{bmatrix} F_{A_1'} \\ F_{N_1'} \end{bmatrix} = \begin{bmatrix} \cos\theta_b & \sin\theta_b \\ -\sin\theta_b & \cos\theta_b \end{bmatrix} \begin{bmatrix} F_{A_1} \\ F_{N_1} \end{bmatrix}$$

where θ_b = bend angle

The total axial and normal force then, are

$$F_A = F_{A_1'} + F_{A_2}$$

$$F_N = F_{N_1'} + F_{N_2}$$

Knowing F_A and F_N the center-of-pressure location can be obtained by the relation

$$\overline{\overline{Z_{CP}}} = \frac{F_{N_2}\left[L-\left(Z_b\cos\theta_b+Z_{CP_2}\right)\right]+ F_{N_1'}\left(L-Z_{CP_1}\cos\theta_b\right)}{F_N}$$

where L = length of the vehicle.

$\overline{\overline{Z_{CP}}}$ = center-of-pressure location measured from the base of the body.

Once the normal force and the center-of-pressure location are known, the moment based on the base of the body is obtained by

$$M = F_N \cdot \overline{\overline{Z_{CP}}}$$

Table 1. Test case conditions

Case	Rn(m)	α	Freestream conditions Alt.(m)	Vel.(m/s)	T∞(K)	Re,Rn	ε	Tw(K)
1a	0.1524	0	83,820	7620	182.16	937.36	0.1745	1000
1b	0.1524	0	70,104	7620	217.37	7029.20	0.0590	1000
2	0.1524	0&5	83,820	7620	182.16	937.36	0.1745	1000
3	0.1524	0	83,820	7620	182.16	937.36	0.1745	1000
4	0.2000	0,10&20	83,820	7620	182.16	1237.30	0.1519	555.5

Table 2. Viscosity curve fit coefficients of individual species.

$$\mu_i = \exp(C_i)\, T_k^{(A_i \ln T_k + B_i)} \text{ ; gm/cm-sec}$$

Species	A	B	C
e-	0.0	0.0	0.0
N2	0.048349	-0.022485	-9.9827
O2	0.038271	0.021076	-9.5986
N	0.0085863	0.6463	-12.581
O	0.020022	0.43094	-11.246
NO	0.042501	-0.018874	-9.6197
N+	0.0085863	0.6463	-12.581
O+	0.3656258	-4.4703	6.46685912
NO+	0.042501	-0.018874	-9.6197
N2+	0.048349	-0.022485	-9.9827
O2+	0.0385788	0.0177	-2.68578034

Table 3. Reaction-rate data for 7 species model after Blottner.

Reaction Equations

r = 1	$O_2 + M_1$	$\rightleftarrows$	$2O + M_1$	
2	$N_2 + M_2$	$\rightleftarrows$	$2N + M_2$	
3	$N_2 + N$	$\rightleftarrows$	$2N + N$	
4	$NO + M_3$	$\rightleftarrows$	$N + O$	$+ M_3$
5	$NO + O$	$\rightleftarrows$	$O_2 + N$	
6	$N_2 + O$	$\rightleftarrows$	$NO + N$	
7	$N + O$	$\rightleftarrows$	$NO^+ + e^-$	

Catalytic Third Bodies Efficiencies Relative to Argon; $Z_{(j-ns),i}$

		O	O_2	NO	N	NO^+	N_2
		i=1	2	3	4	5	6
(j-ns) = 1	M_1	25	9	1	1	0	2
2	M_2	1	1	1	0	0	2.5
3	M_3	20	1	20	20	0	1
4	e^-	0	0	0	0	1	0

Table 3. Reaction-rate data for 7 species model after Blottner (concluded)

Reaction Rate Constants

$k_{f_r} = T_k^{C2_r} \exp (CO_r - C1_r/T_k)$

$k_{b_r} = T_k^{D2_r} \exp (DO_r - D1_r/T_k)$ T_k degrees Kelvin

Reaction No.	CO_r	$\exp (CO_r)$	$C1_r$	$C2_r$	DO_r	$\exp (DO_r)$	$D1_r$	$D2_r$
r = 1	42.7302	3.61×10^{18}	59,400	-1	35.6407	3.01×10^{15}	0	-1/2
2	39.7963	1.92×10^{17}	113,100	-1/2	36.9275	1.09×10^{16}	0	-1/2
3	52.0800	4.15×10^{22}	113,100	-3/2	49.1959	2.32×10^{21}	0	-3/2
4	47.4305	3.97×10^{20}	75,600	-3/2	46.0617	1.01×10^{20}	0	-3/2
5	21.8801	3.18×10^{9}	19,700	1	27.5933	9.63×10^{11}	3600	1/2
6	31.8431	6.75×10^{13}	37,500	0	30.3391	1.50×10^{13}	0	0
7	22.9238	9.03×10^{9}	32,400	1/2	44.3369	1.80×10^{19}	0	-1

Table 4. Reaction-rate data for 7 species model after Kang and Dunn.

NO.	REACTION	FORWARD RATE COEFF, k_F	BACKWARD RATE COEFF, k_B	THIRD BODY, M
	FORWARD DIRECTION	cm^3/mole sec	cm^3/mole sec OR $cm^6/mole^2$ sec	——
1	$O_2 + M \rightarrow 2O + M$	$3.6 \times 10^{18} T^{-1.0} \exp(-5.95 \times 10^4/T)$	$3.0 \times 10^{15} T^{-0.5}$	N, NO
2	$N_2 + M \rightarrow 2N + M$	$1.9 \times 10^{17} T^{-0.5} \exp(-1.13 \times 10^5/T)$	$1.1 \times 10^{16} T^{-0.5}$	O, NO, O_2
3	$NO + M \rightarrow N + O + M$	$3.9 \times 10^{20} T^{-1.5} \exp(-7.55 \times 10^4/T)$	$1.0 \times 10^{20} T^{-1.5}$	O_2, N_2
4	$O + NO \rightarrow N + O_2$	$3.2 \times 10^{9} T^{1} \exp(-1.97 \times 10^4/T)$	$1.3 \times 10^{10} T^{1.0} \exp(-3.58 \times 10^3/T)$	
5	$O + N_2 \rightarrow N + NO$	$7.0 \times 10^{13} \exp(-3.8 \times 10^4/T)$	1.56×10^{13}	
6	$N + N_2 \rightarrow N + N + N$	$4.085 \times 10^{22} T^{-1.5} \exp(-1.13 \times 10^5/T)$	$2.27 \times 10^{21} T^{-1.5}$	
7	$O + N \rightarrow NO^+ + e^-$	$(1.4 \pm 0.4) \times 10^6 T^{1.5} \exp(-3.19 \times 10^4/T)$	$(6.7 \pm 2.3) \times 10^{21} T^{-1.5}$	
8	$O_2 + O \rightarrow 2O + O$	$9.0 \times 10^{19} T^{-1.0} \exp(-5.95 \times 10^4/T)$	$7.5 \times 10^{16} T^{-0.5}$	
9	$O_2 + O_2 \rightarrow 2O + O_2$	$3.24 \times 10^{19} T^{-1.0} \exp(-5.95 \times 10^4/T)$	$2.7 \times 10^{16} T^{-0.5}$	
10	$O_2 + N_2 \rightarrow 2O + N_2$	$7.2 \times 10^{18} T^{-1.0} \exp(-5.95 \times 10^4/T)$	$6.0 \times 10^{15} T^{-0.5}$	
11	$N_2 + N_2 \rightarrow 2N + N_2$	$4.7 \times 10^{17} T^{-0.5} \exp(-1.13 \times 10^5/T)$	$2.72 \times 10^{16} T^{-0.5}$	
12	$NO + M \rightarrow N + O + M$	$7.8 \times 10^{20} T^{-1.5} \exp(-7.55 \times 10^4/T)$	$2.0 \times 10^{20} T^{-1.5}$	O, N, NO

Table 5. Reaction-rate data for 11 species model after Kang and Dunn.

NO.	REACTION	FORWARD RATE COEFF, k_F	BACKWARD RATE COEFF, k_B	THIRD BODY, M
	FORWARD DIRECTION	cm^3/mole sec	cm^3/mole sec OR cm^6/$mole^2$ sec	——
1	$O_2 + M \rightarrow 2O + M$	$3.6 \times 10^{18} T^{-1.0} \exp(-5.95 \times 10^4/T)$	$3.0 \times 10^{15} T^{-0.5}$	N, NO
2	$N_2 + M \rightarrow 2N + M$	$1.9 \times 10^{17} T^{-0.5} \exp(-1.13 \times 10^5/T)$	$1.1 \times 10^{16} T^{-0.5}$	O, NO, O_2
3	$NO + M \rightarrow N + O + M$	$3.9 \times 10^{20} T^{-1.5} \exp(-7.55 \times 10^4/T)$	$1.0 \times 10^{20} T^{-1.5}$	O_2, N_2
4	$O + NO \rightarrow N + O_2$	$3.2 \times 10^9 T^1 \exp(-1.97 \times 10^4/T)$	$1.3 \times 10^{10} T^{1.0} \exp(-3.58 \times 10^3/T)$	
5	$O + N_2 \rightarrow N + NO$	$7.0 \times 10^{13} \exp(-3.8 \times 10^4/T)$	1.56×10^{13}	
6	$N + N_2 \rightarrow N + N + N$	$4.085 \times 10^{22} T^{-1.5} \exp(-1.13 \times 10^5/T)$	$2.27 \times 10^{21} T^{-1.5}$	
7	$O + N \rightarrow NO^+ + e^-$	$(1.4 \pm 0.4) \times 10^6 T^{1.5} \exp(-3.19 \times 10^4/T)$	$(6.7 \pm 2.3) \times 10^{21} T^{-1.5}$	
8	$O + e^- \rightarrow O^+ + e^- + e^-$	$(3.6 \pm 1.2) \times 10^{31} T^{-2.91} \exp(-1.58 \times 10^5/T)$	$(2.2 \pm 0.7) \times 10^{40} T^{-4.5}$	
9	$N + e^- \rightarrow N^+ + e^- + e^-$	$(1.1 \pm 0.4) \times 10^{32} T^{-3.14} \exp(-1.69 \times 10^5/T)$	$(2.2 \pm 0.7) \times 10^{40} T^{-4.5}$	
10	$O + O \rightarrow O_2^+ + e^-$	$(1.6 \pm 0.4) \times 10^{17} T^{-0.98} \exp(-8.08 \times 10^4/T)$	$(8.0 \pm 2.0) \times 10^{21} T^{-1.5}$	
11	$O + O_2^+ \rightarrow O_2 + O^+$	$2.92 \times 10^{18} T^{-1.11} \exp(-2.8 \times 10^4/T)$	$7.8 \times 10^{11} T^{0.5}$	
12	$N_2 + N^+ \rightarrow N + N_2^+$	$2.02 \times 10^{11} T^{0.81} \exp(-1.3 \times 10^4/T)$	$7.8 \times 10^{11} T^{0.5}$	
13	$N + N \rightarrow N_2^+ + e^-$	$(1.4 \pm 0.3) \times 10^{13} \exp(-6.78 \times 10^4/T)$	$(1.5 \pm 0.5) \times 10^{22} T^{-1.5}$	
14	$O_2 + N_2 \rightarrow NO + NO^+ + e^-$	$1.38 \times 10^{20} T^{-1.84} \exp(-1.41 \times 10^5/T)$	$1.0 \times 10^{24} T^{-2.5}$	

Table 5. Reaction-rate data for 11 species model after Kang and Dunn (concluded)

NO.	REACTION	FORWARD RATE COEFF, k_F	BACKWARD RATE COEFF, k_B	THIRD BODY, M
	FORWARD DIRECTION	cm^3/mole sec	cm^3/mole sec OR $cm^6/mole^2$ sec	——
15	$NO + N_2 \rightarrow NO^+ + e^- + N_2$	$2.2 \times 10^{15} T^{-0.35} \exp(-1.08 \times 10^5/T)$	$2.2 \times 10^{26} T^{-2.5}$	
16	$O + NO^+ \rightarrow NO + O^+$	$3.63 \times 10^{15} T^{-0.6} \exp(-5.08 \times 10^4/T)$	1.5×10^{13}	
17	$N_2 + O^+ \rightarrow O + N_2^+$	$3.4 \times 10^{19} T^{-2.0} \exp(-2.3 \times 10^4/T)$	$2.48 \times 10^{19} T^{-2.2}$	
18	$N + NO^+ \rightarrow NO + N^+$	$1.0 \times 10^{19} T^{-0.93} \exp(-6.1 \times 10^4/T)$	4.8×10^{14}	
19	$O_2 + NO^+ \rightarrow NO + O_2^+$	$1.8 \times 10^{15} T^{0.17} \exp(-3.3 \times 10^4/T)$	$1.8 \times 10^{13} T^{0.5}$	
20	$O + NO^+ \rightarrow O_2 + N^+$	$1.34 \times 10^{13} T^{0.31} \exp(-7.727 \times 10^4/T)$	1.0×10^{14}	
21	$NO + O_2 \rightarrow NO^+ + e^- + O_2$	$8.8 \times 10^{15} T^{-0.35} \exp(-1.08 \times 10^5/T)$	$8.8 \times 10^{26} T^{-2.5}$	
22	$O_2 + O \rightarrow 2O + O$	$9.0 \times 10^{19} T^{-1.0} \exp(-5.95 \times 10^4/T)$	$7.5 \times 10^{16} T^{-0.5}$	
23	$O_2 + O_2 \rightarrow 2O + O_2$	$3.24 \times 10^{19} T^{-1.0} \exp(-5.95 \times 10^4/T)$	$2.7 \times 10^{16} T^{-0.5}$	
24	$O_2 + N_2 \rightarrow 2O + N_2$	$7.2 \times 10^{18} T^{-1.0} \exp(-5.95 \times 10^4/T)$	$6.0 \times 10^{15} T^{-0.5}$	
25	$N_2 + N_2 \rightarrow 2N + N_2$	$4.7 \times 10^{17} T^{-0.5} \exp(-1.13 \times 10^5/T)$	$2.72 \times 10^{16} T^{-0.5}$	
26	$NO + M \rightarrow N + O + M$	$7.8 \times 10^{20} T^{-1.5} \exp(-7.55 \times 10^4/T)$	$2.0 \times 10^{20} T^{-1.5}$	O, N, NO

Table 6. Aerodynamic forces and moments for multiconics.[a]

Case	α = 0 CA	α = 5 CA	CN	CM	ZCP/L	CMα	CNα
2 NOL[b] PG	0.10032	0.10447	0.08793	-0.04406	0.5011	0.5049	1.0077
2 VSL PG	0.37193	0.36669	0.11851	-0.06391	0.5393	0.7324	1.3581
2 VSL NEQ	0.38580	0.41000	0.12794	-0.06914	0.5404	0.7923	1.4662
3 NOL[a] PG	0.08718	0.08732	0.02654	-0.01073	0.4043	0.3074	0.7604
3 VSL PG	0.33334	0.34714	0.03743	-0.01503	0.4015	0.4306	1.0724

[a] 7 species model

[b] Inviscid code

Table 7. Aerodynamic forces and moments for bent biconic.[a]

	α	CA	CN	CM[b]	$\overline{\overline{ZCP}}/L$[b]
Perfect gas	0	0.24316	0.15179	-0.06843	0.4508
Perfect gas	10	0.33425	0.39959	-0.18266	0.4571
NEQ. FCW	0	0.27199	0.13590	-0.06516	0.4793
NEQ. FCW	10	0.34733	0.38397	-0.17680	0.4605
NEQ. FCW	20	0.44640	0.69780	-0.30881	0.4425
EQBM	0	0.26910	0.14155	-0.06766	0.4779

[a] 7 Species model

[b] Measured from end of the body

Table 8. Computing times[a] for test case 1

α Deg.	Alt. (m)	Method	Flow Type	ξ from - to	Grid size[b] ξ-steps	η-pts	ζ-planes	Time[c] (m:s)	ratio
0	83,820	VSLNEQ	NSS	0.0 - 20.0	57	51	1	4:43	1.00
0	83,820	VSLNEQ	SS	0.0 - 20.0	57	51	1	5:42	1.21
0	83,820	VSL7S	NSS	0.0 - 20.0	57	51	1	5:19	1.13
0	83,820	VSL7S	SS	0.0 - 20.0	57	51	1	6:04	1.28
0	70,104	VSLNEQ	NSS	0.0 - 20.0	57	51	1	5:15	1.11
0	70,104	VSL7S	SS	0.0 - 20.0	57	51	1	6:07	1.30

[a]CPU time on IBM 370/3032, H=OPT2 compiler.

[b]Core requirements: VSL7S. 255 kbytes.
VSLNEQ. 265 kbytes.

[c]Reference: 83.82 km NSS VSLNEQ for α = 0 deg.

Table 9. Computing times[a] for test cases 2,3 and 4

Case[b]	α Deg.	ξ from - to	Grid size of ξ-steps	η-pts	ζ-planes	Time (m:s)	ratio[c]
2 PG	0	0.0 - 21.0	50	101	1	0:21	1.00
2 PG	5	0.0 - 21.0	52	101	9	2:42	7.71
2 NEQ	0	0.0 - 21.0	50	51	1	1:46	1.00
2 NEQ	5	0.0 - 21.0	52	51	9	11:51	6.71
3 PG	0	0.0 - 31.5	70	101	1	0:28	1.00
3 NEQ	0	0.0 - 31.5	70	51	1	2:31	1.00
3 NEQ[d]	0	0.0 - 31.5	70	51	1	7:00	2.78
4 PG	0	0.0 - 31.5	60	101	9	3:23	1.00
4 PG	10	0.0 - 31.5	62	101	9	3:06	0.92
4 PG	20	0.0 - 31.5	65	101	9	2:58	0.87
4 NEQ	0	0.0 - 31.5	64	51	9	15:07	1.00
4 NEQ	10	0.0 - 31.5	62	51	9	18:33	1.23
4 NEQ	20	0.0 - 31.5	67	51	9	15:48	1.05
4 EQBM[e]	0	0.0 - 31.5	62	101	9	26:28	1.75[f]

a CPU time on IBM 370/3081, H=OPT2 compiler
b Case 2 = 9/4 Straight biconic
Case 3 = 9/0/5 Sphere-cone-cylinder-flare
Case 4 = 12.84/7 Bent biconic
c α = 0 for each case is taken as the reference
d 11 Species model
e Table-look-up procedure
f Nonequlibrium α = 0 is taken as reference

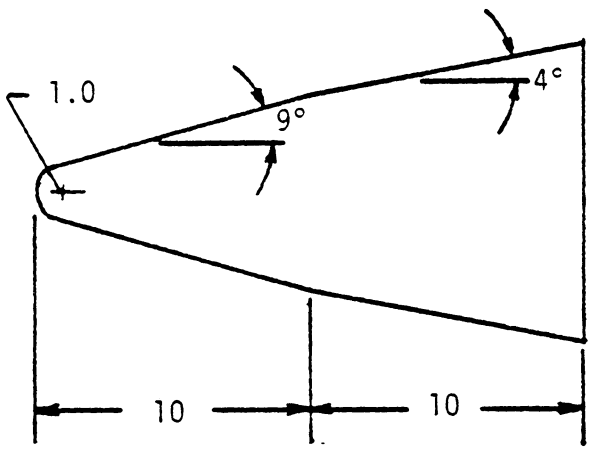

Fig. 1. Schematic of biconic

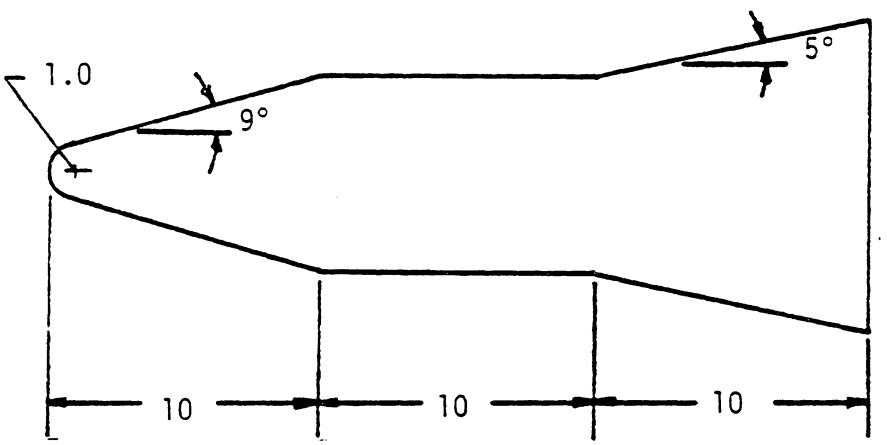

Fig. 2. Schematic of sphere-cone-cylinder-flare

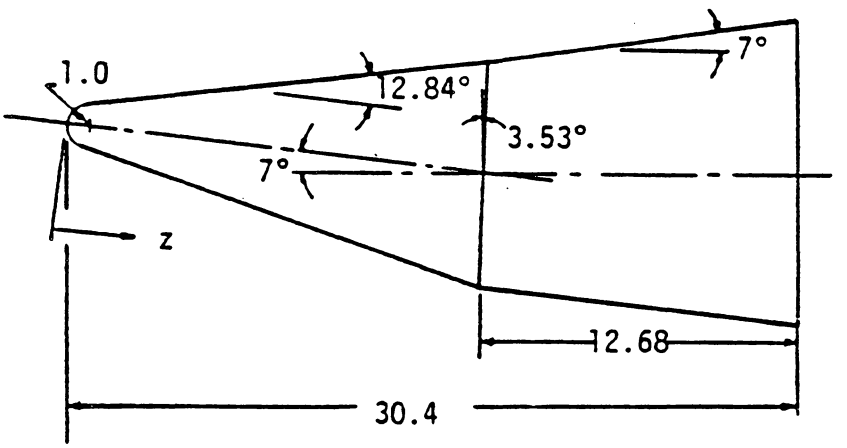

Fig. 3. Schematic of bent-biconic

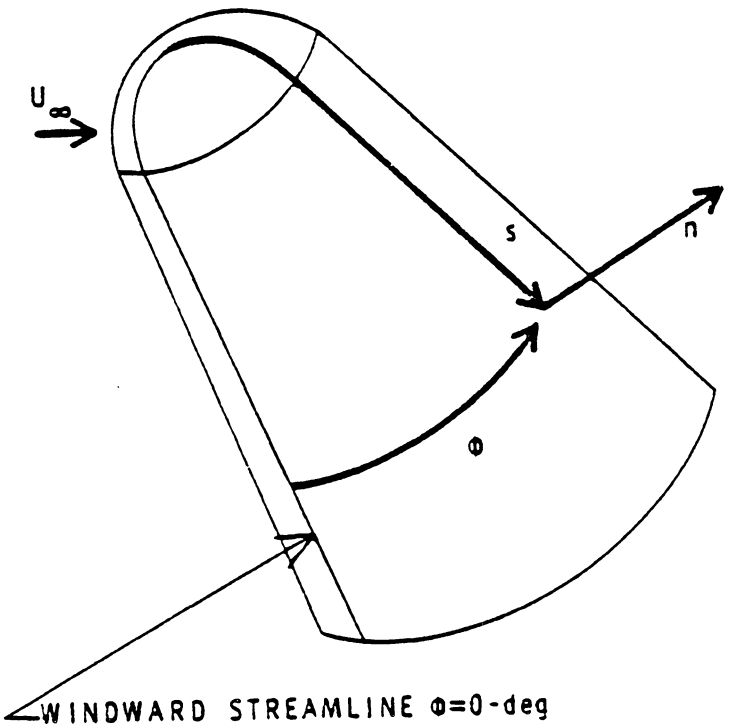

Fig. 4. Coordinate System.

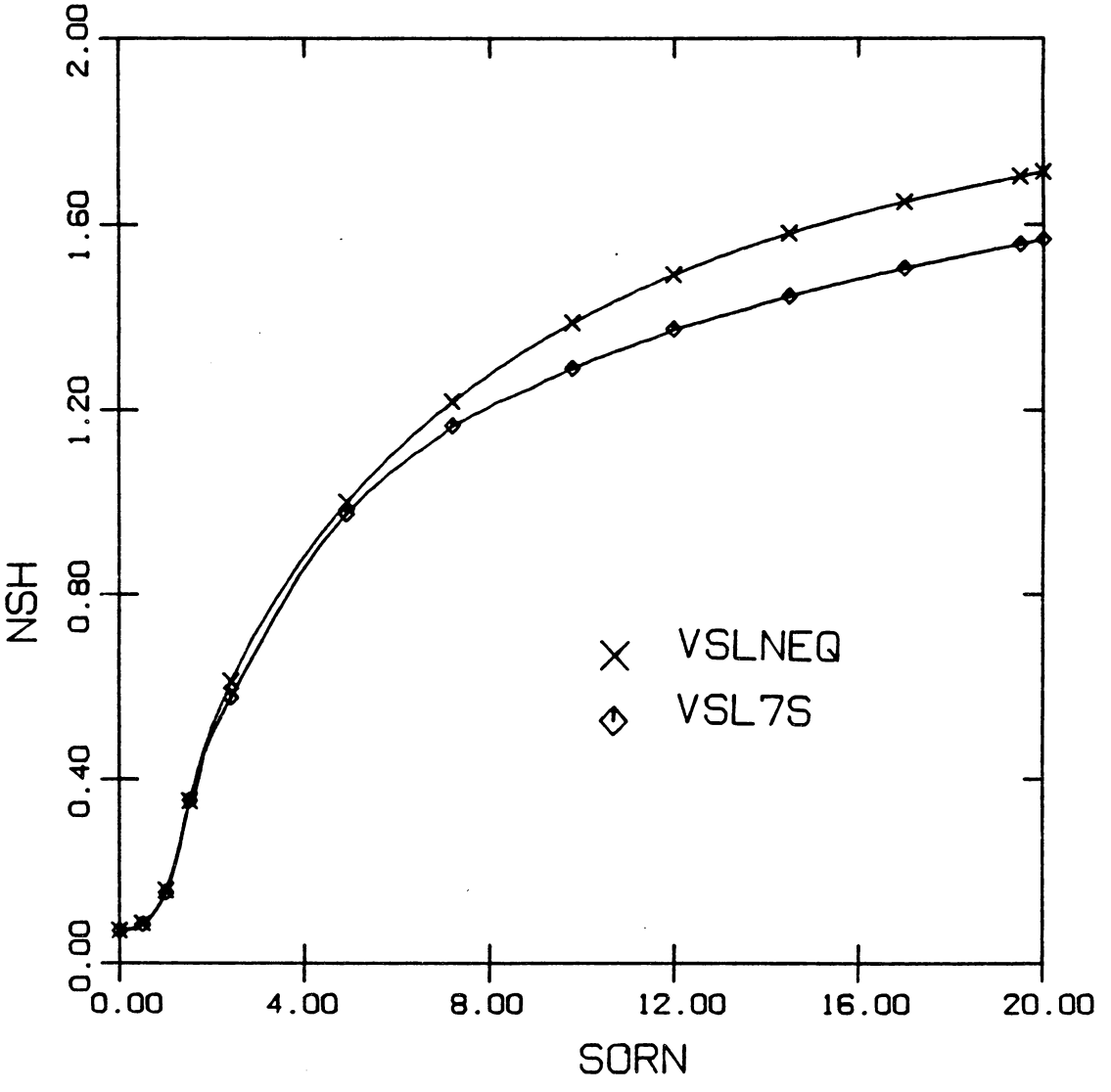

Fig. 5. Shock Stand-off Distance for case 1 at α = 0 deg.

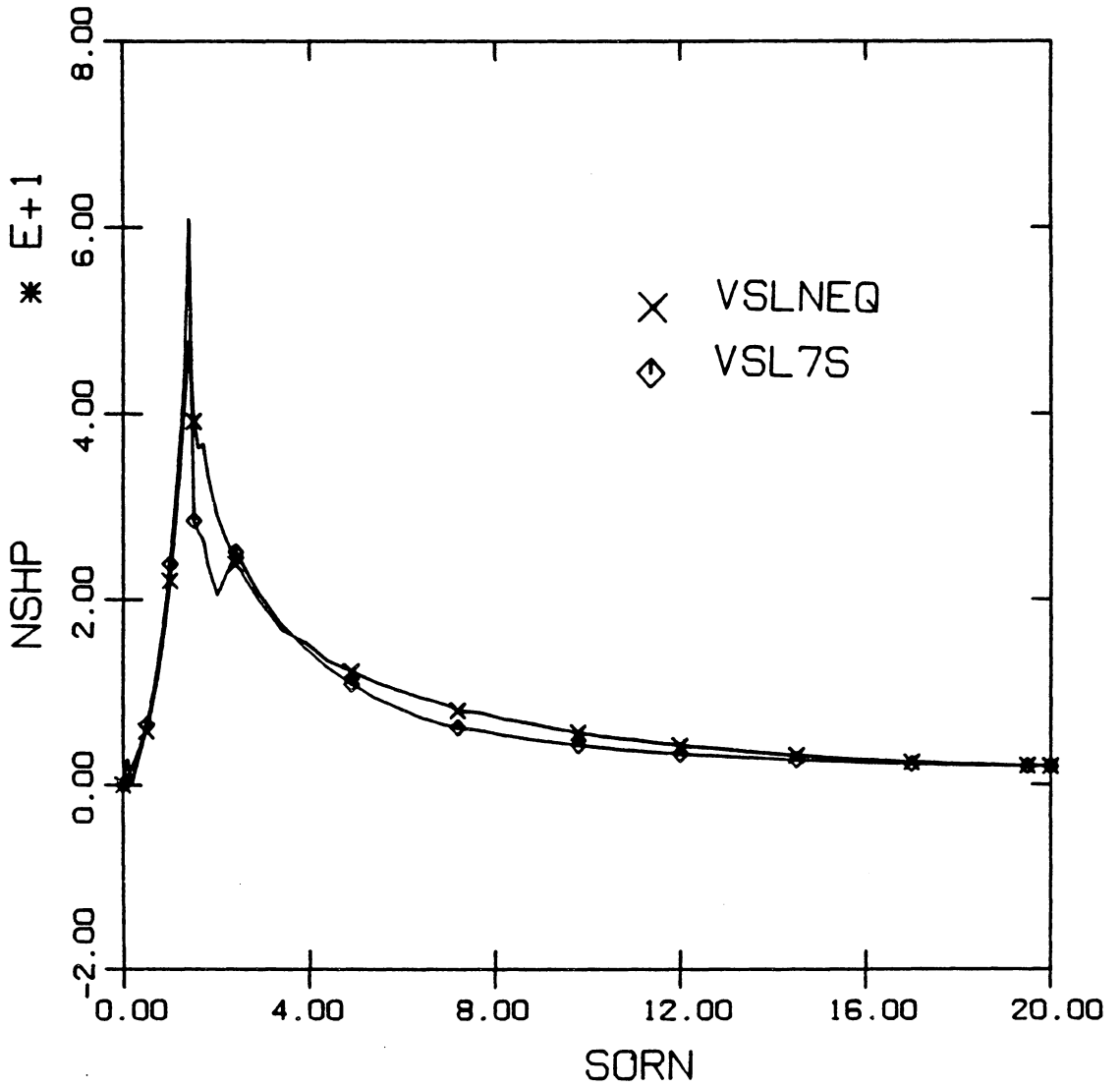

Fig. 6. Shock Slope Distribution for case 1 at α = 0 deg.

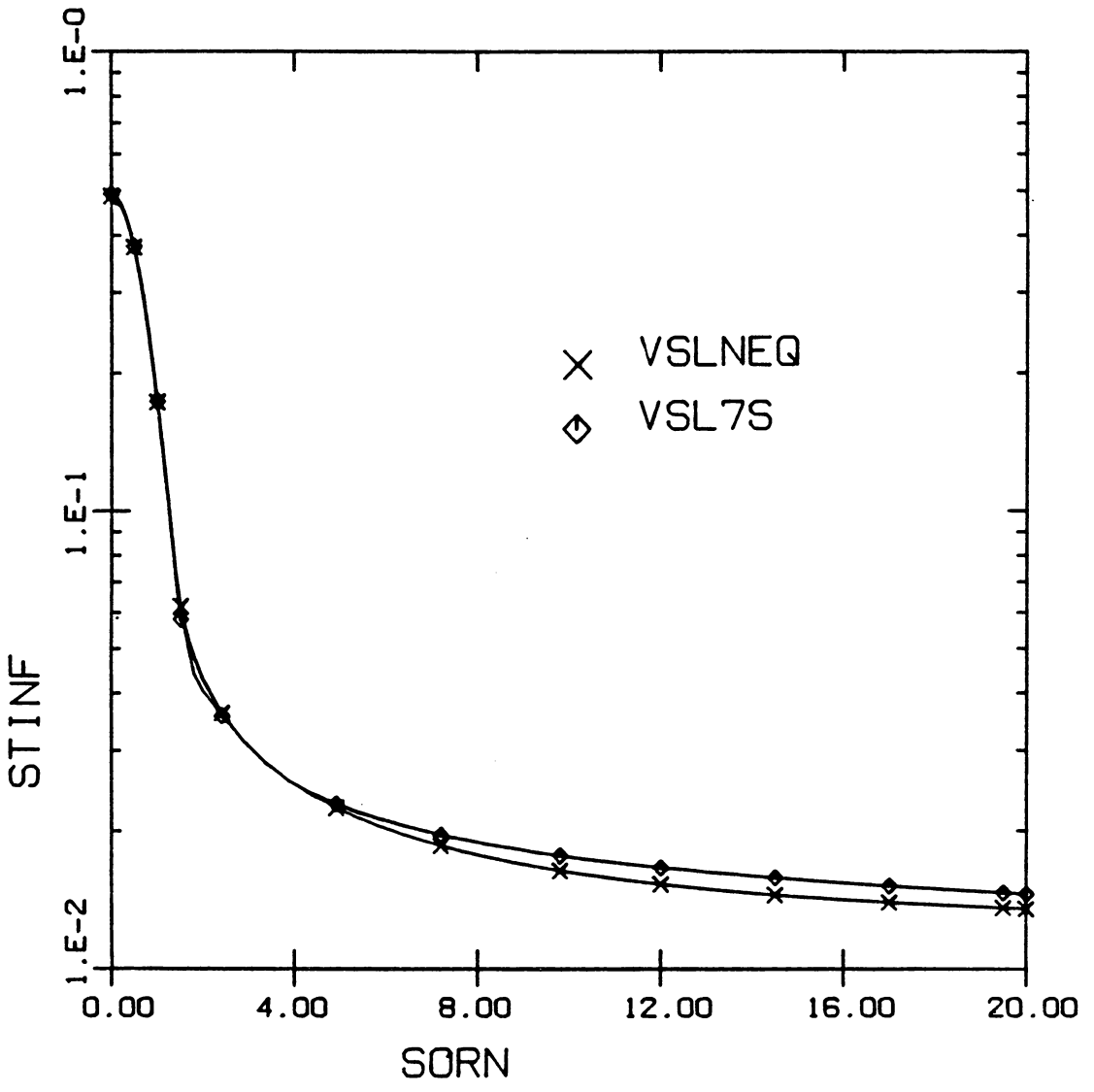

Fig. 7. Surface Heat-Transfer Distribution for case 1 at α = 0 deg.

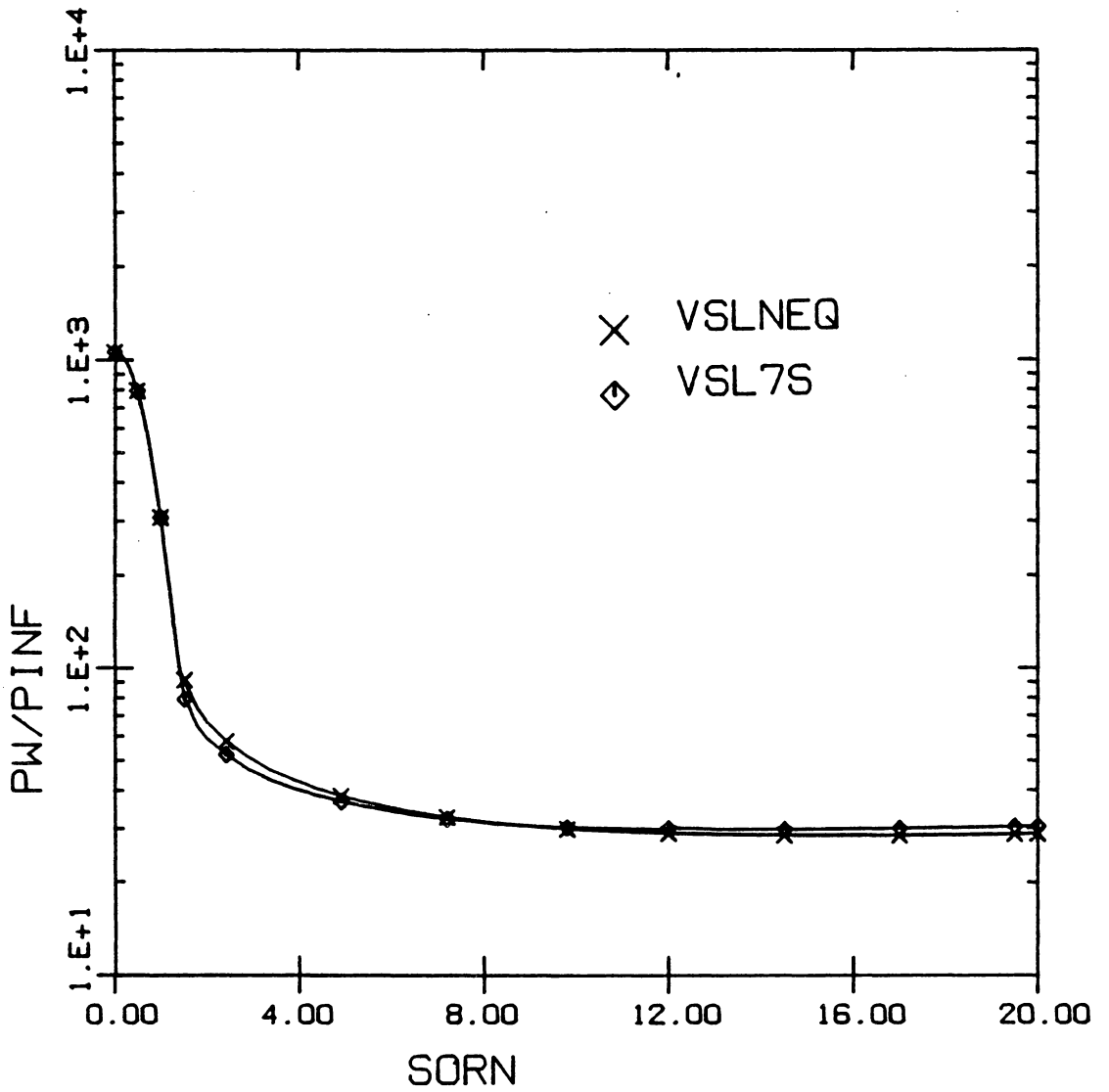

Fig. 8. Surface Pressure Distribution for case 1 at α = 0 deg.

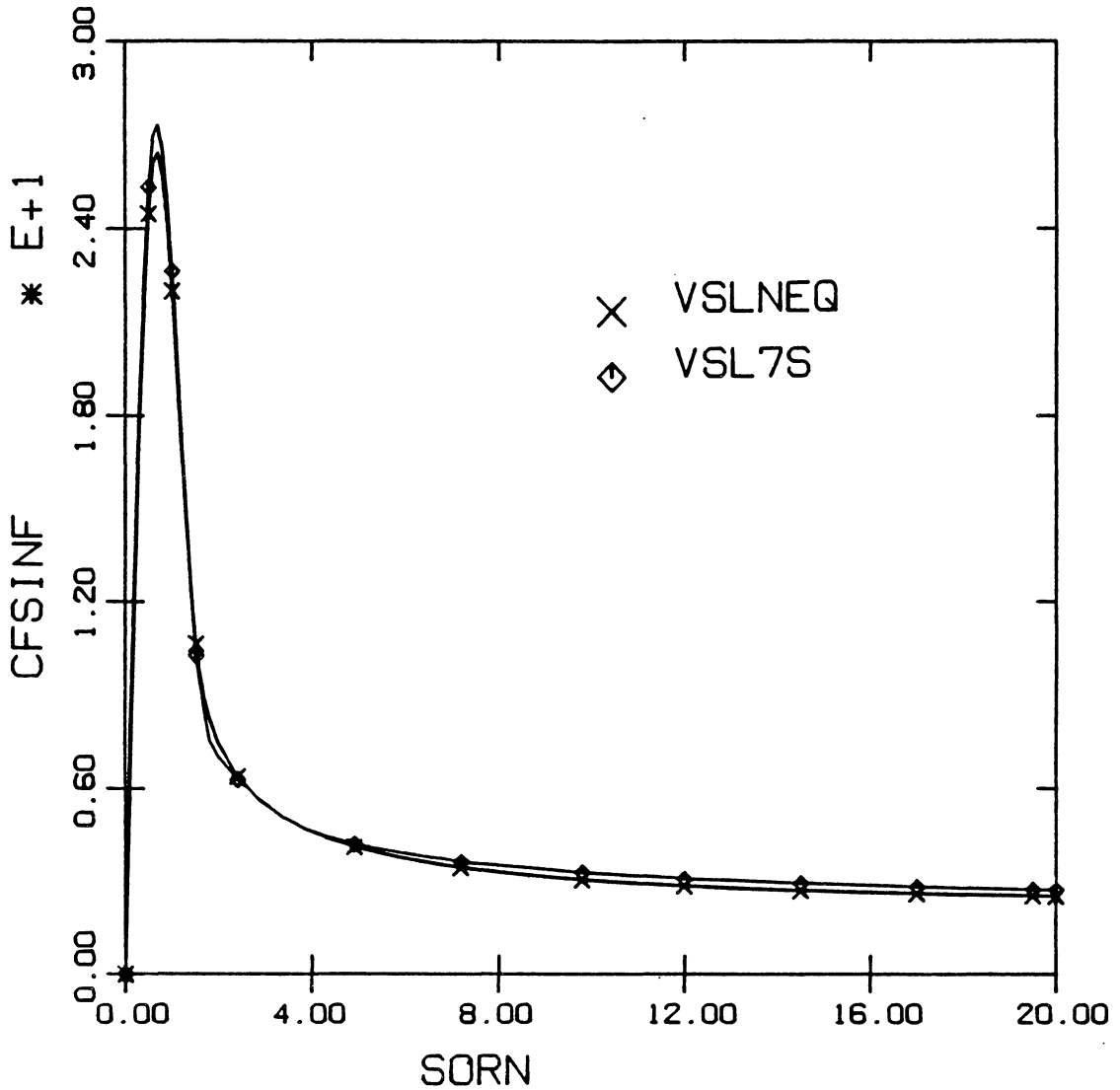

Fig. 9. Streamwise skin-friction distribution for case 1 at α = 0 deg.

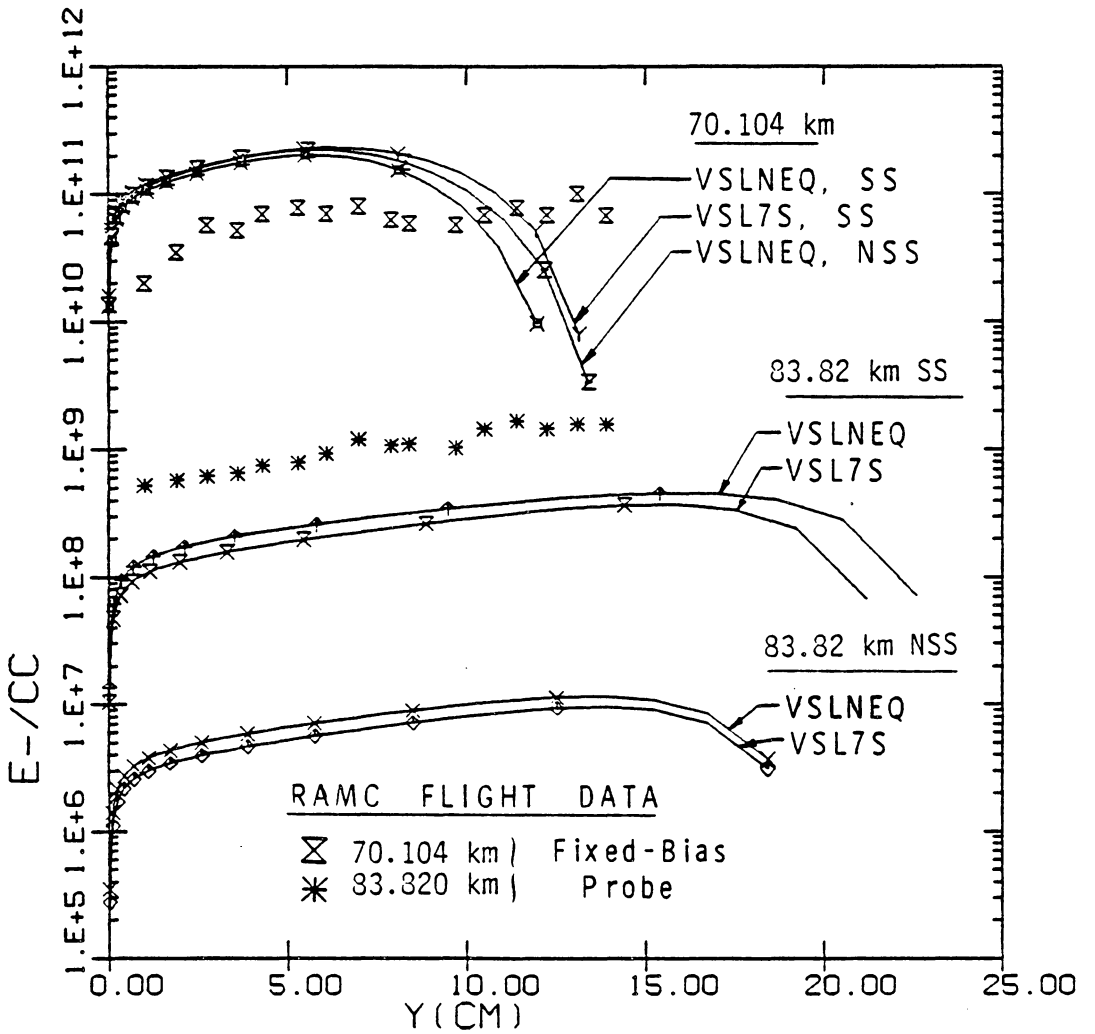

Fig.10. Electron number density for case 1 at s/Rn* = 8.8 at α = 0 deg.

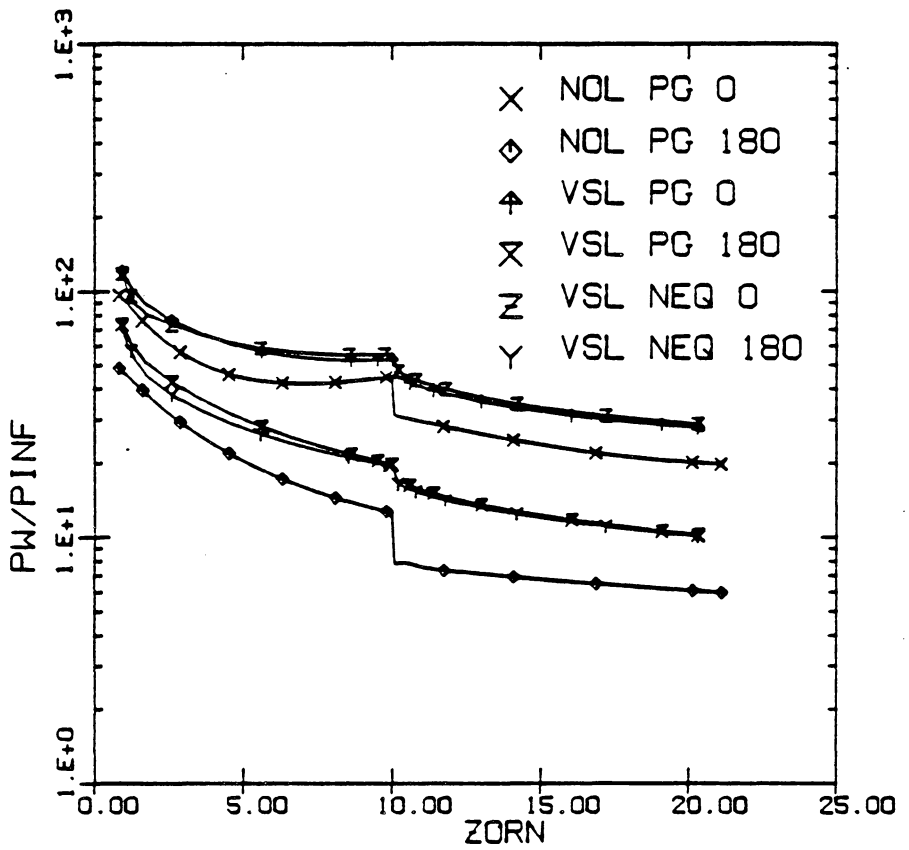

Fig.11. Surface pressure distribution for Case 2 at α = 5 deg.

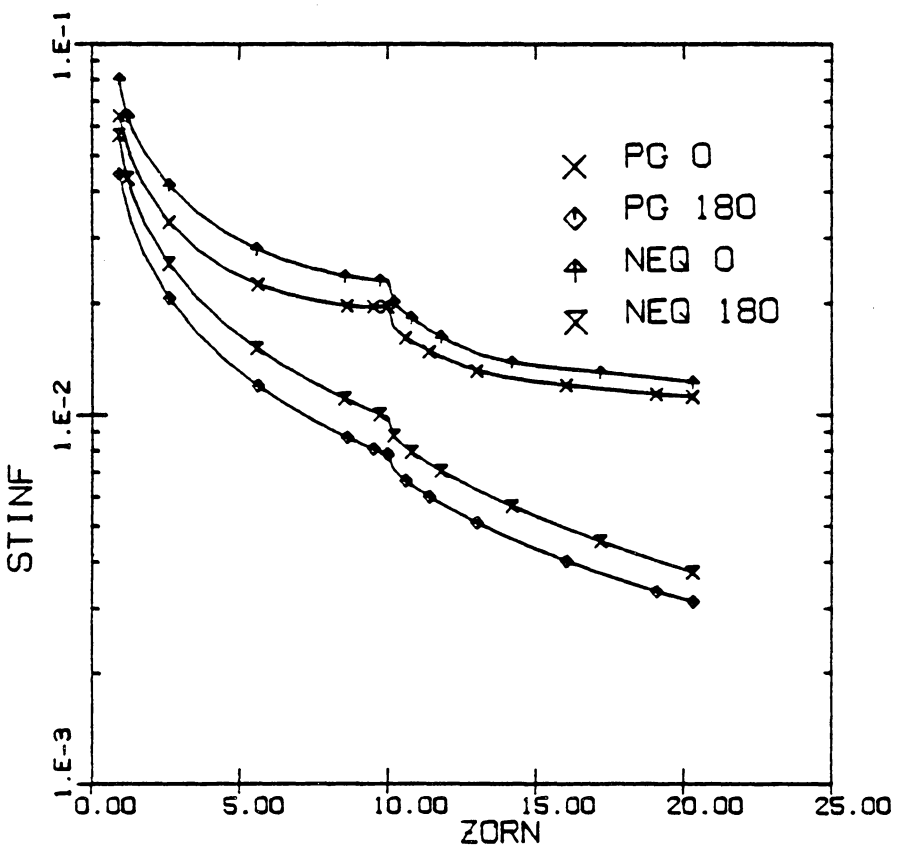

Fig.12. Surface heat-transfer distribution for Case 2 at α = 5 deg.

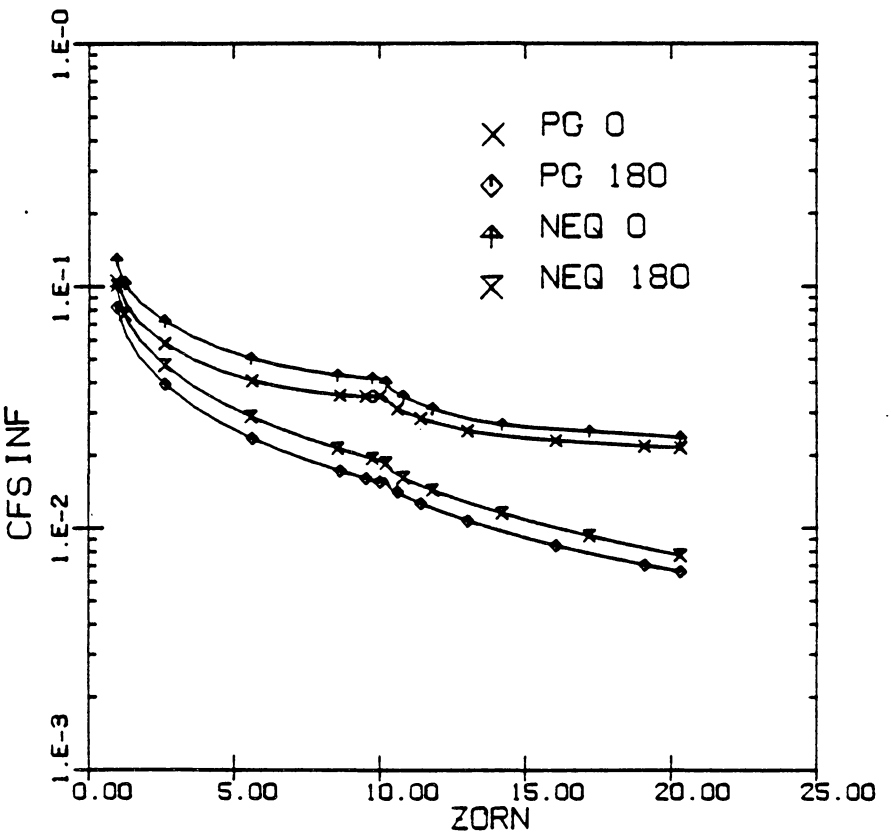

Fig.13. Streamwise skin-friction distribution for Case 2 at α = 5 deg.

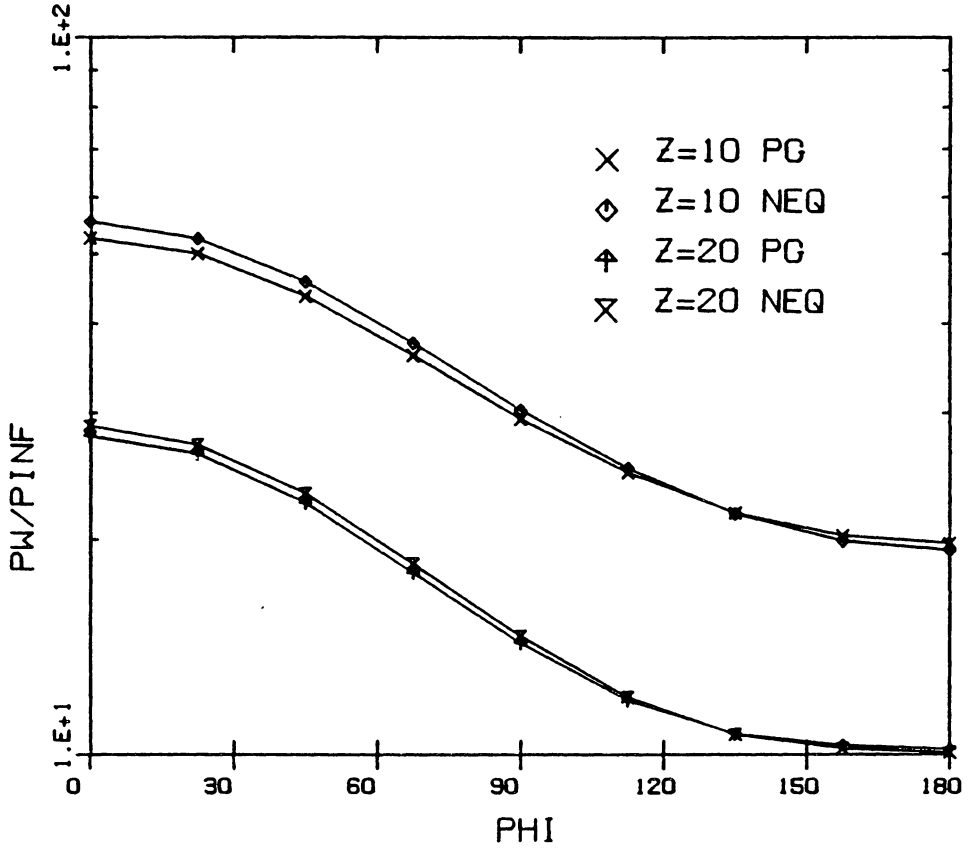

Fig.14. Circumferential surface pressure distribution for Case 2 at α = 5 deg.

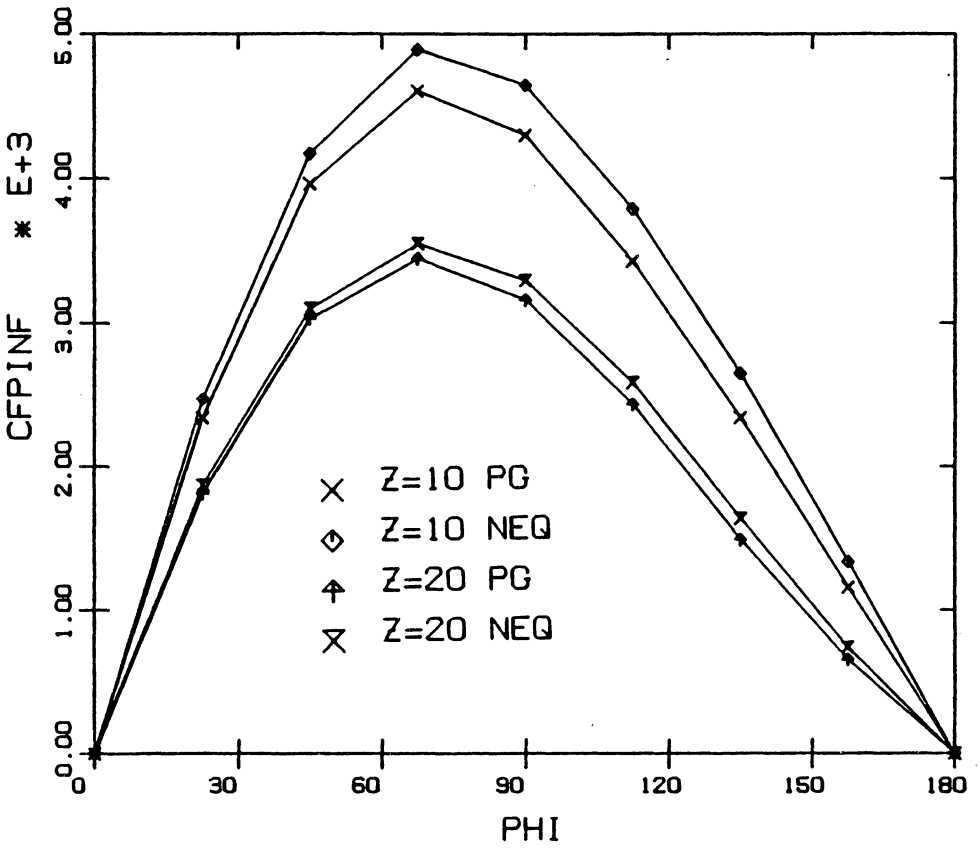

Fig.15. Circumferential skin-friction distribution for Case 2 at α = 5 deg.

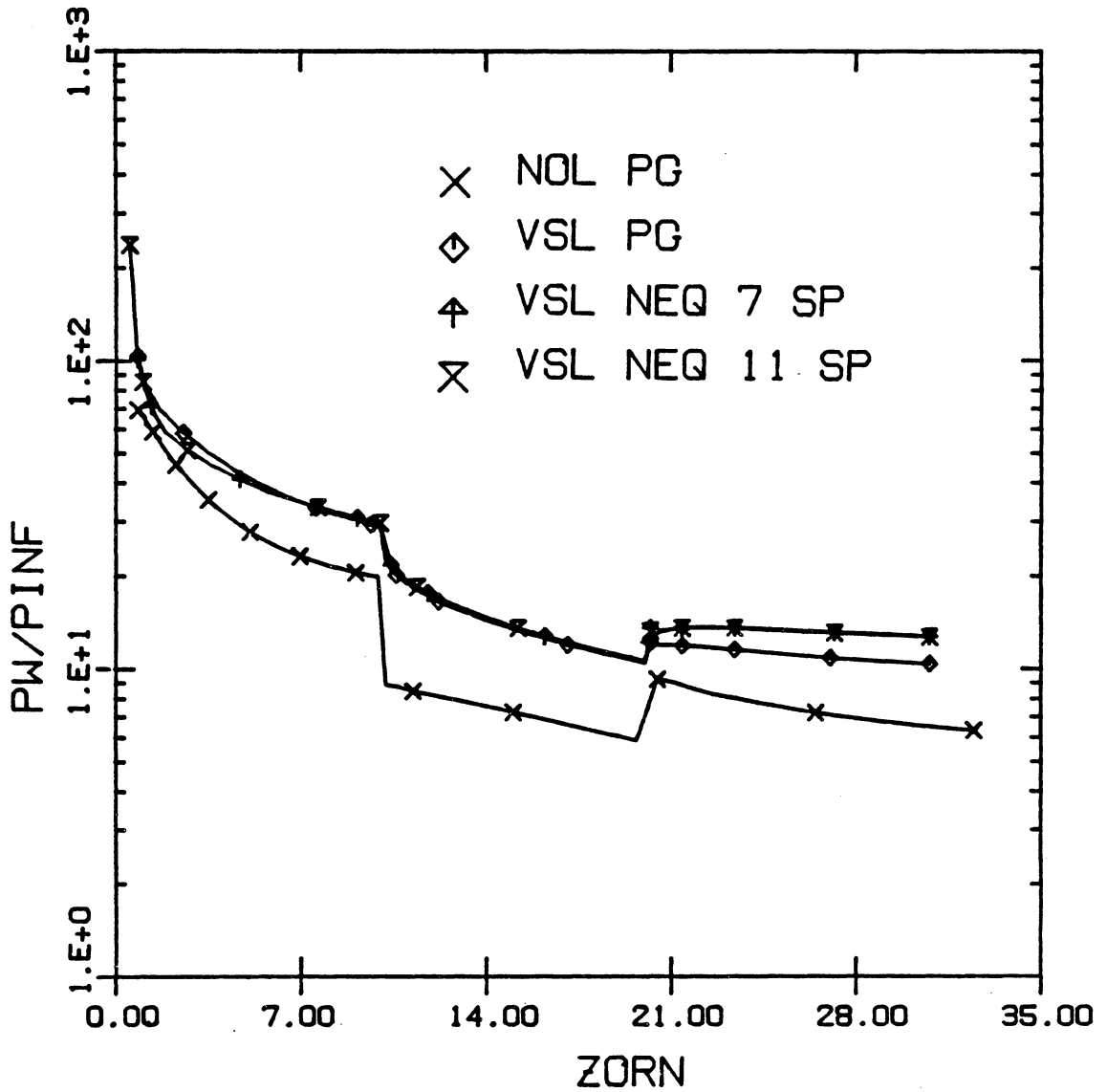

Fig.16. Surface pressure distribution for Case 3 at α = 0 deg.

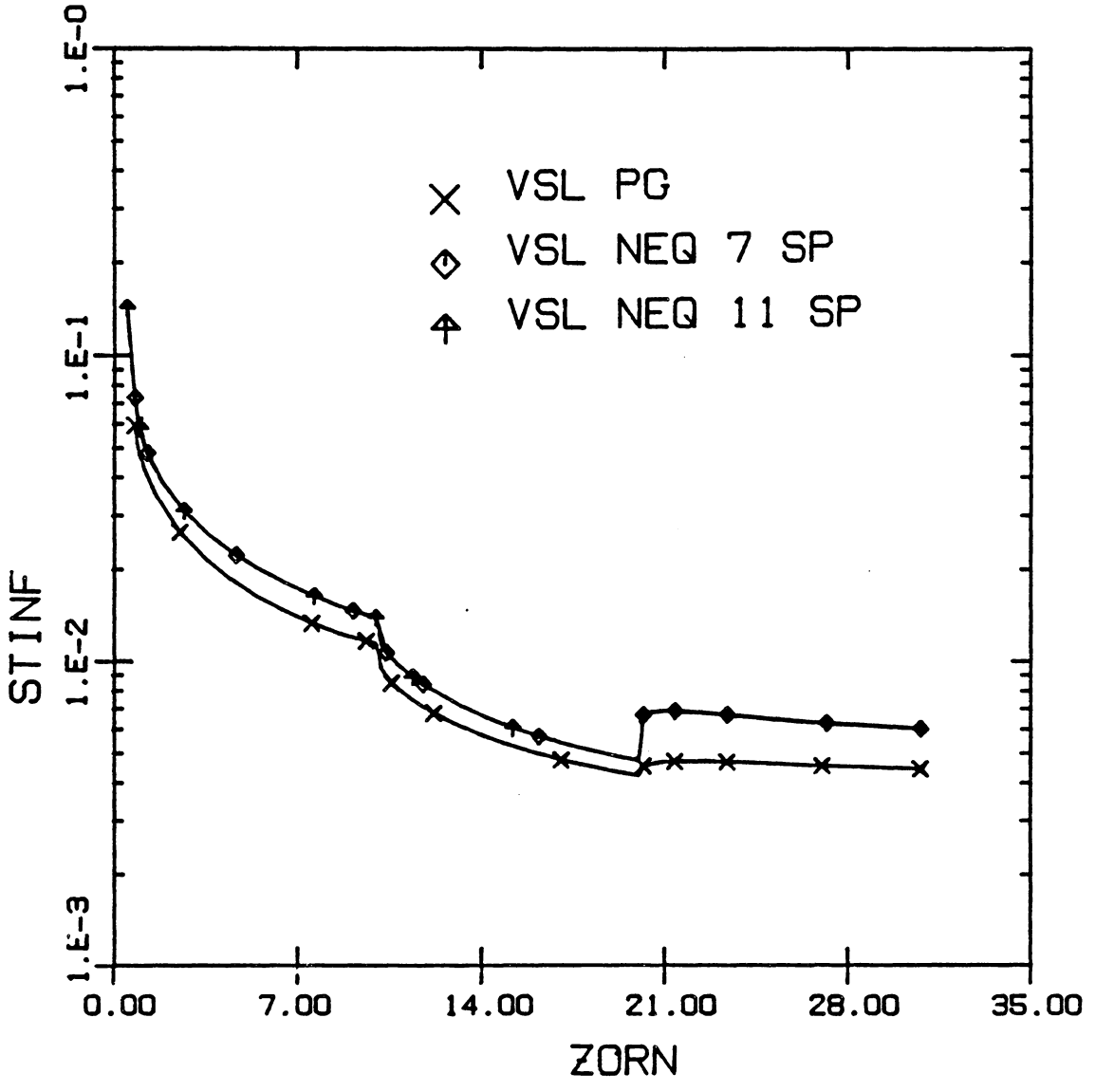

Fig.17. Surface heat-transfer distribution for Case 3 at α = 0 deg.

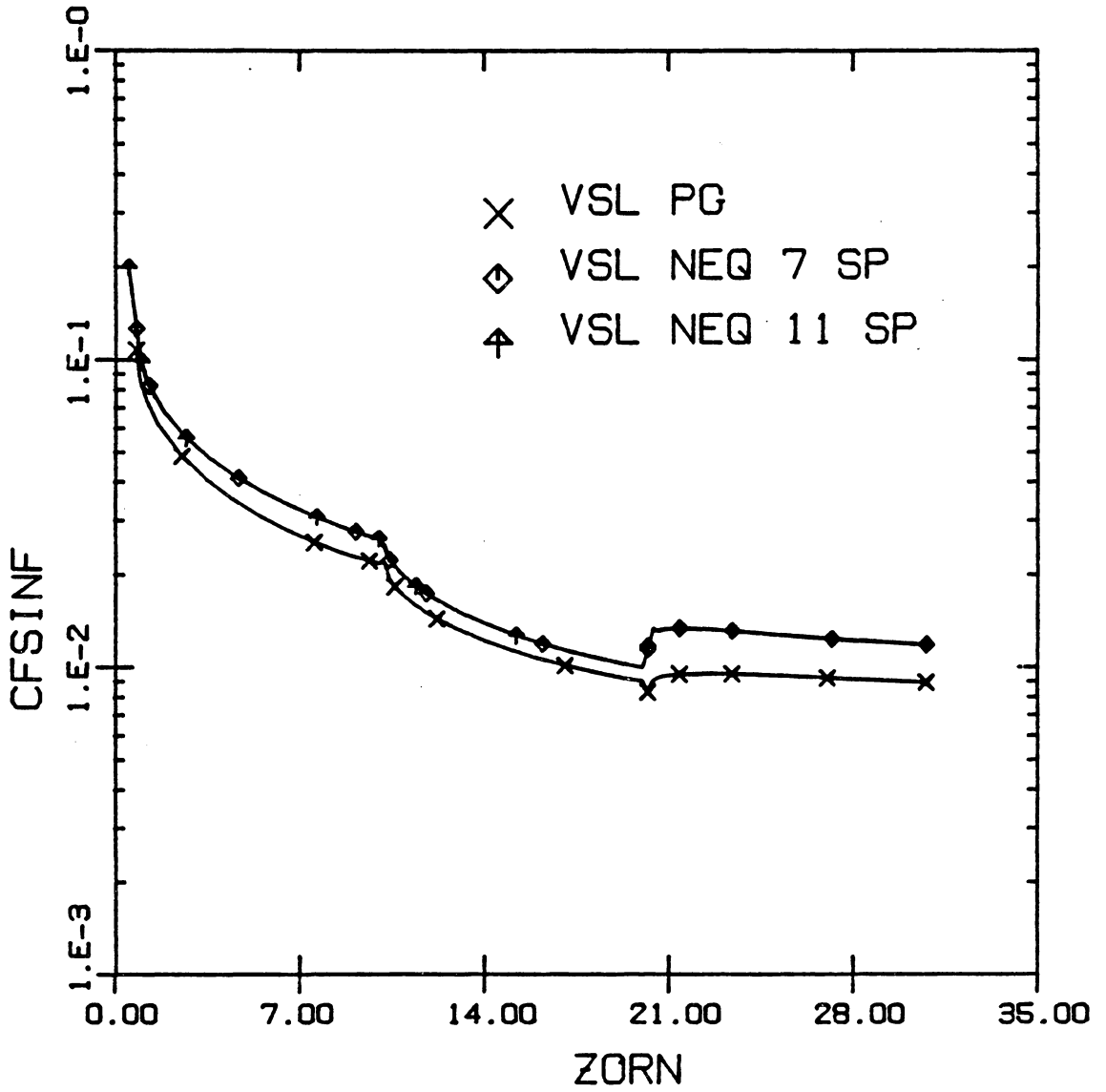

Fig.18. Streamwise skin-friction distribution for Case 3 at α = 0 deg.

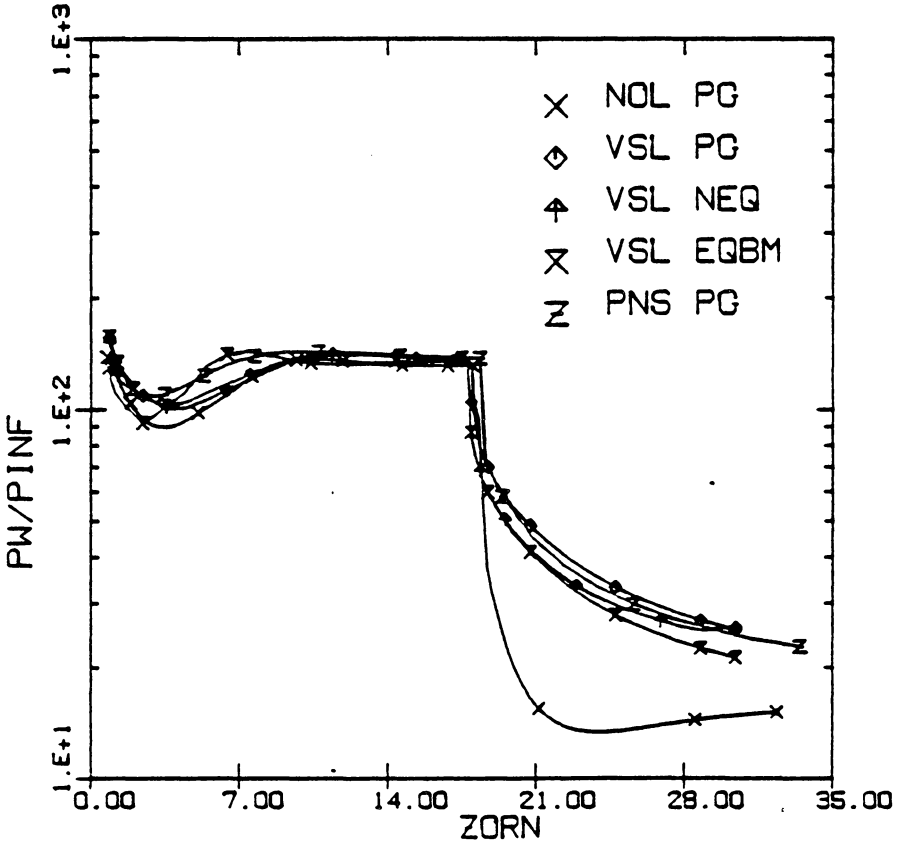

Fig.19a. Surface pressure distribution for Case 4 at $\alpha = 0$, $\phi = 0$ deg.

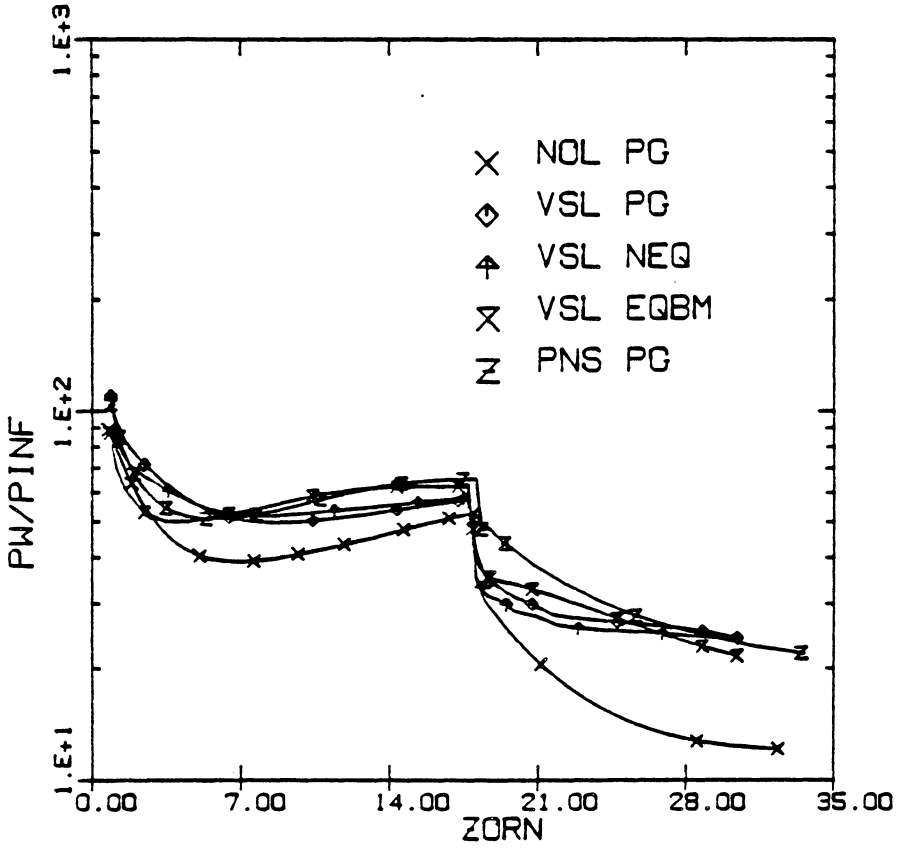

Fig.19b. Surface pressure distribution for Case 4 at α = 0, ϕ = 90 deg.

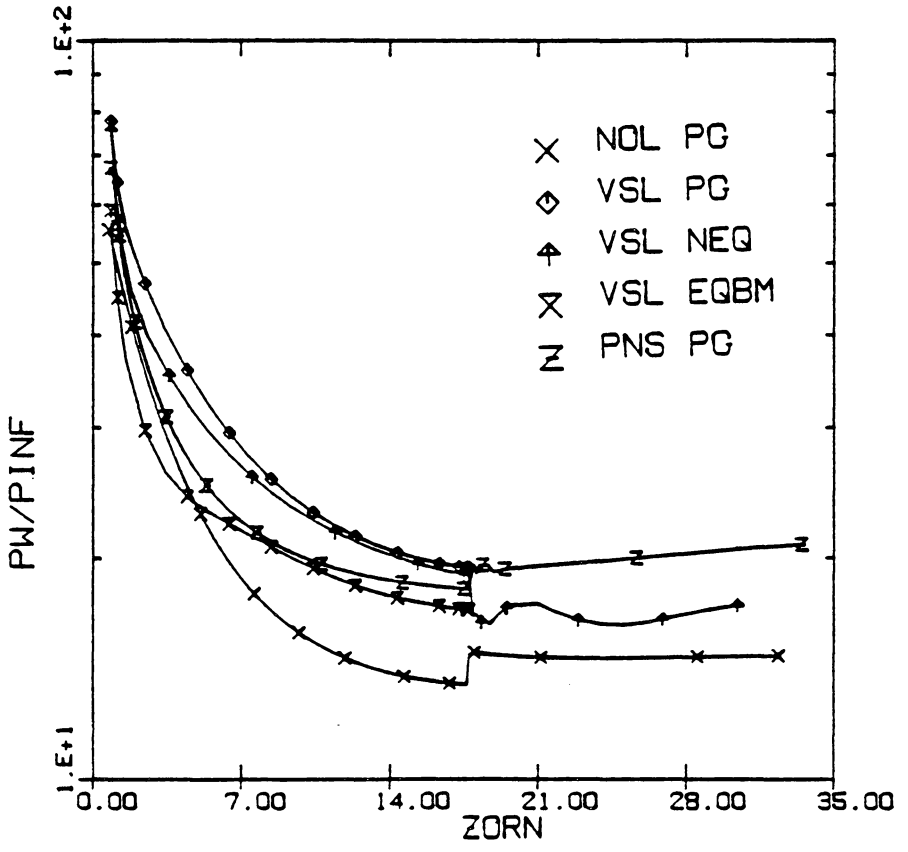

Fig.19c. Surface pressure distribution for Case 4 at α = 0, ϕ = 180 deg.

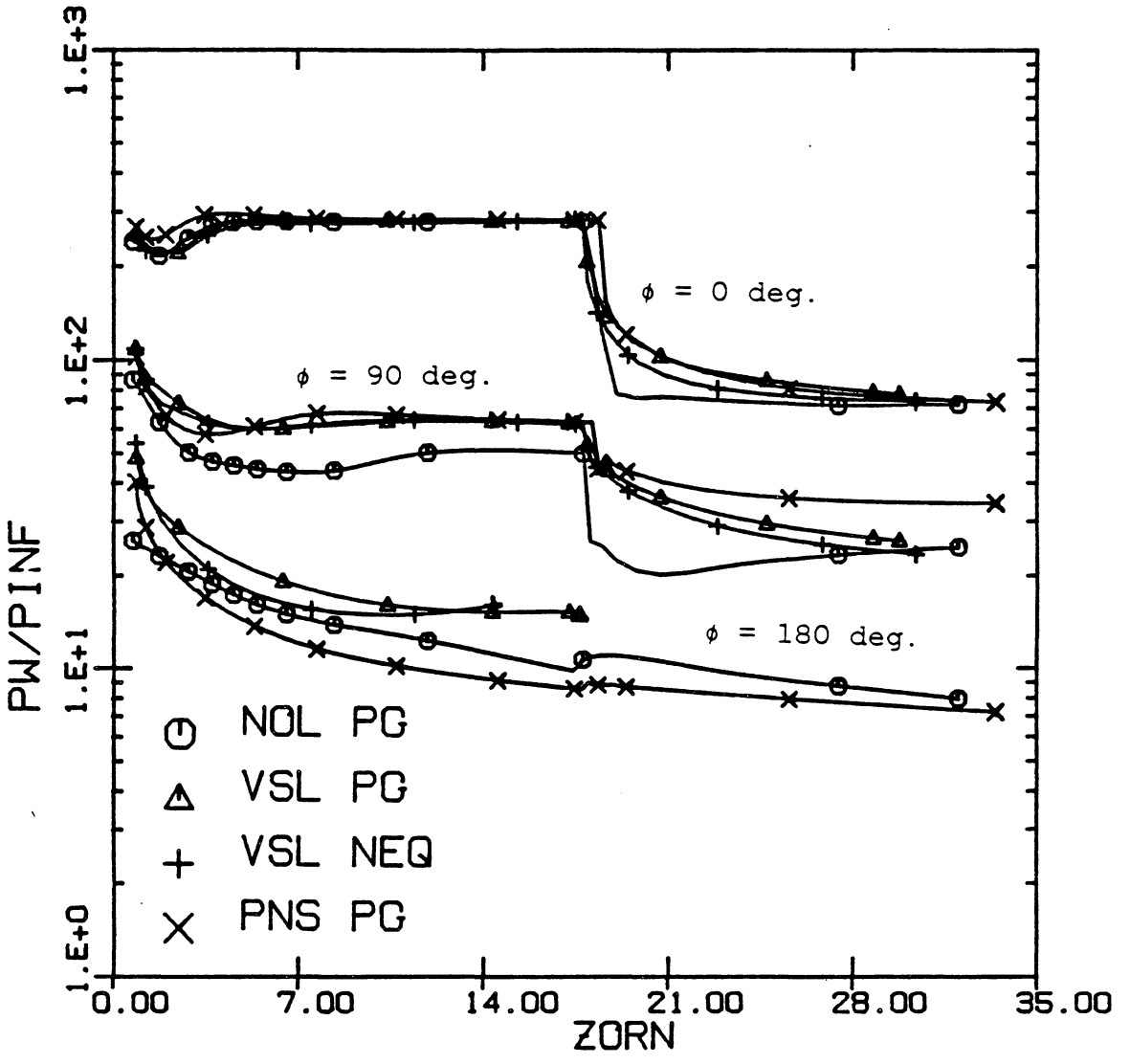

Fig.20. Surface pressure distribution for Case 4 at α = 10 deg.

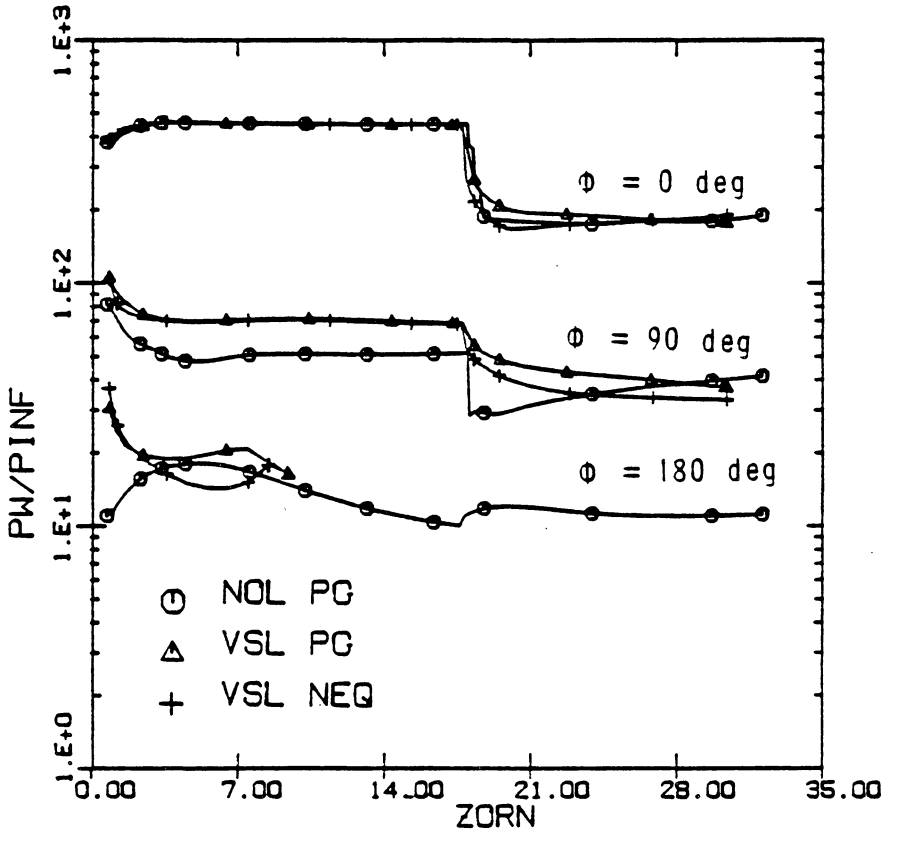

Fig.21. Surface pressure distribution for Case 4 at α = 20 deg.

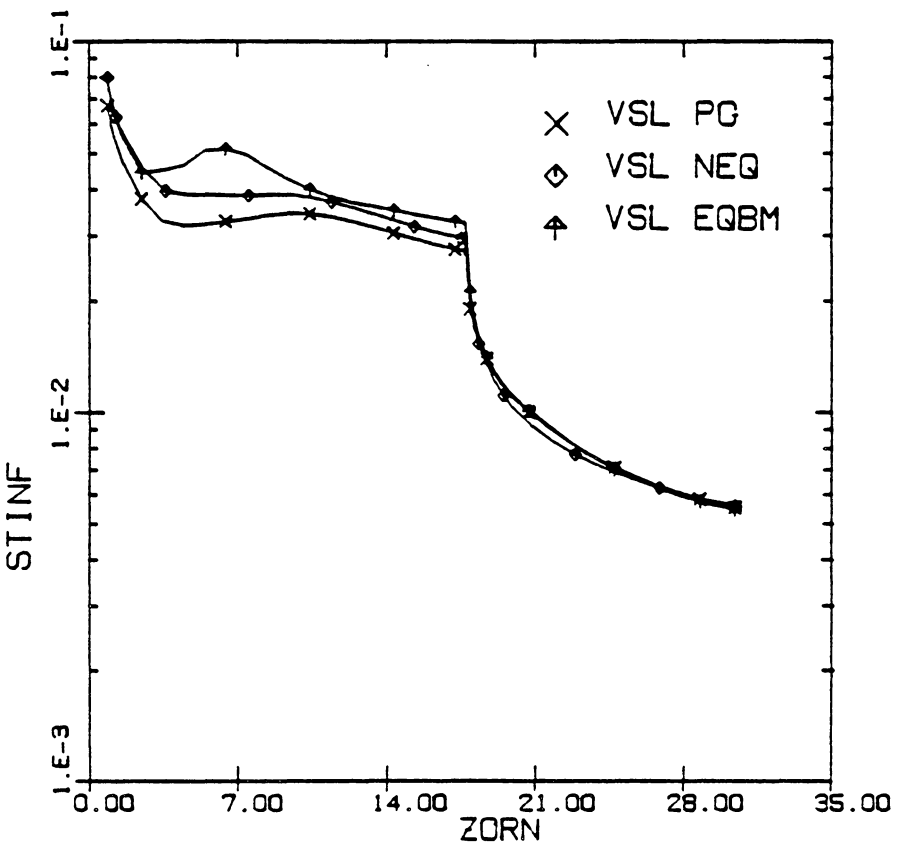

Fig.22a. Surface heat-transfer distribution for Case 4 at α = 0 deg., ϕ = 0 deg.

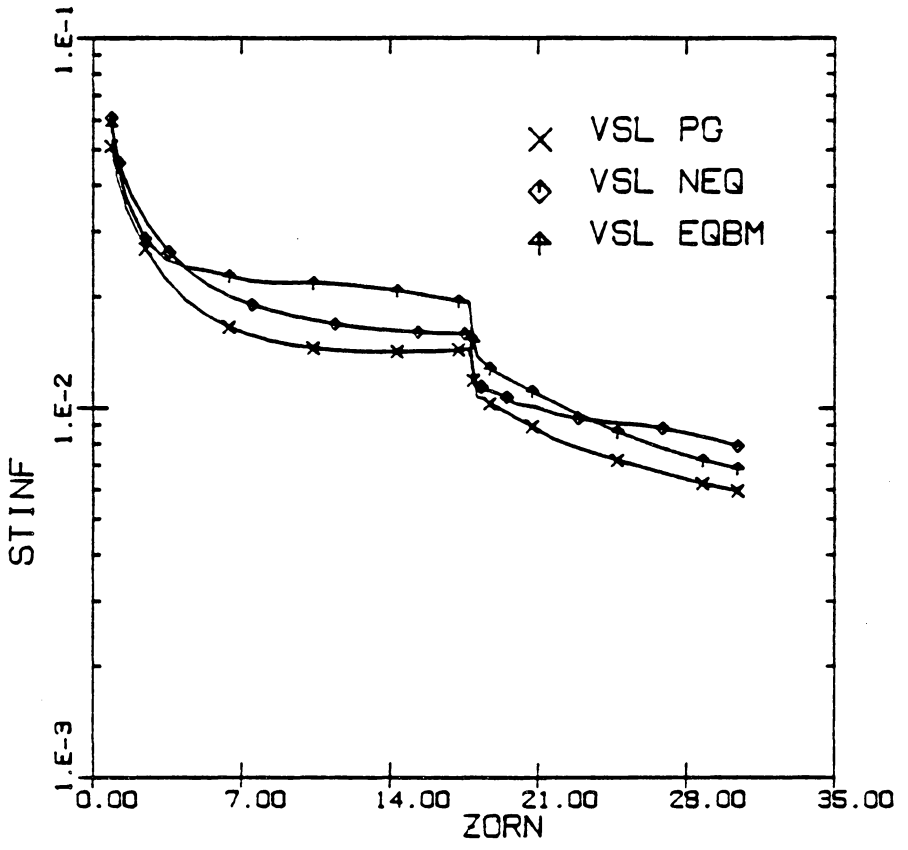

Fig.22b. Surface heat-transfer distribution for Case 4 at α = 0 deg., ϕ = 90 deg.

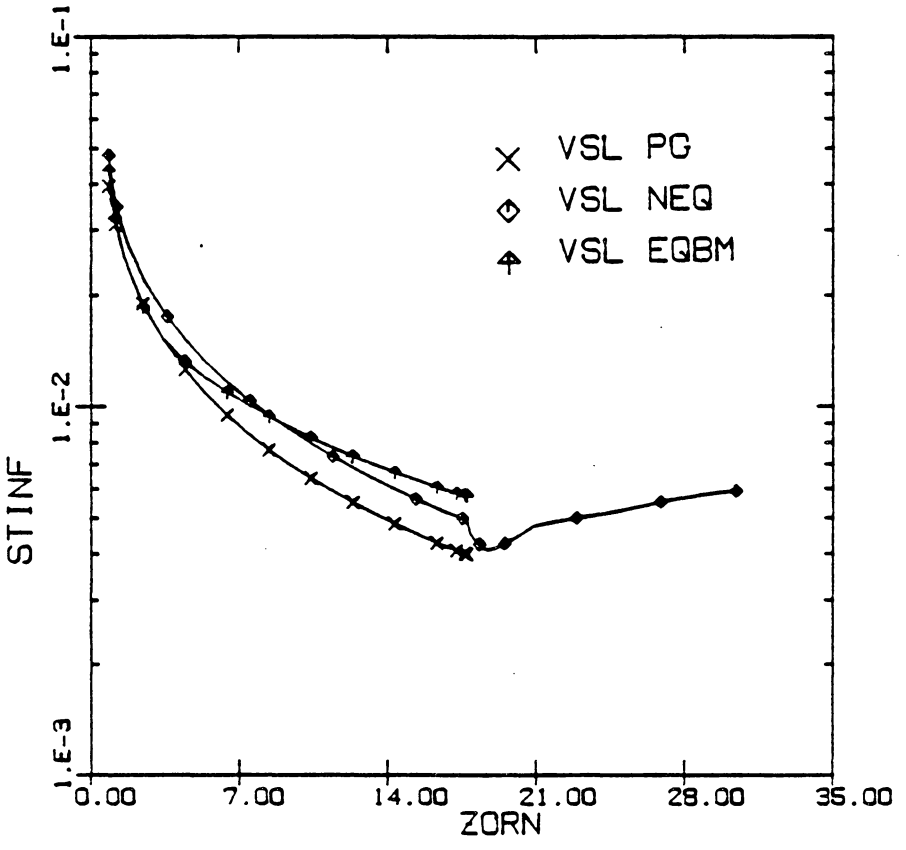

Fig.22c. Surface heat-transfer distribution for Case 4 at α = 0 deg., ϕ = 180 deg.

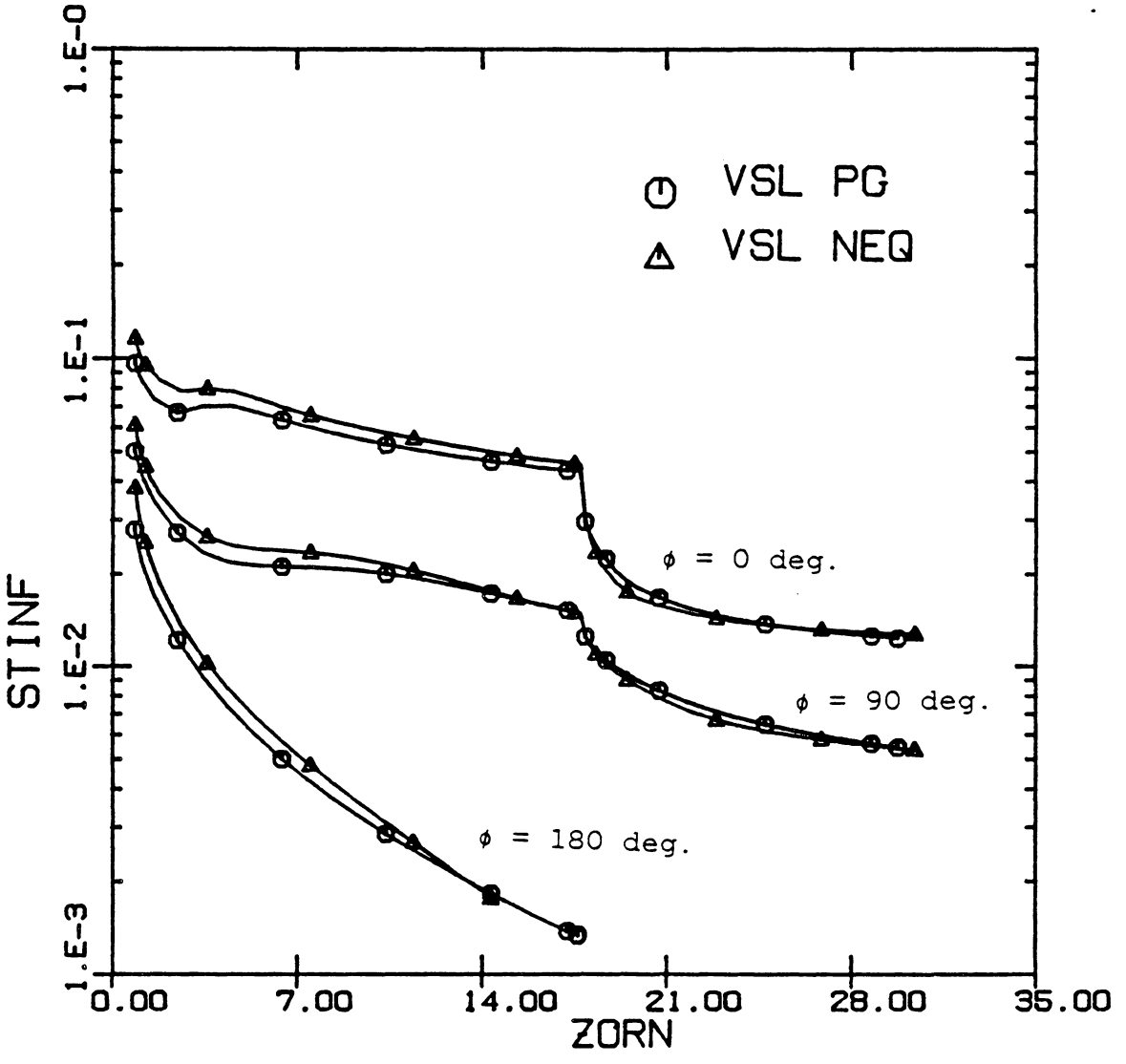

Fig.23. Surface heat-transfer distribution for Case 4 for α = 10 deg.

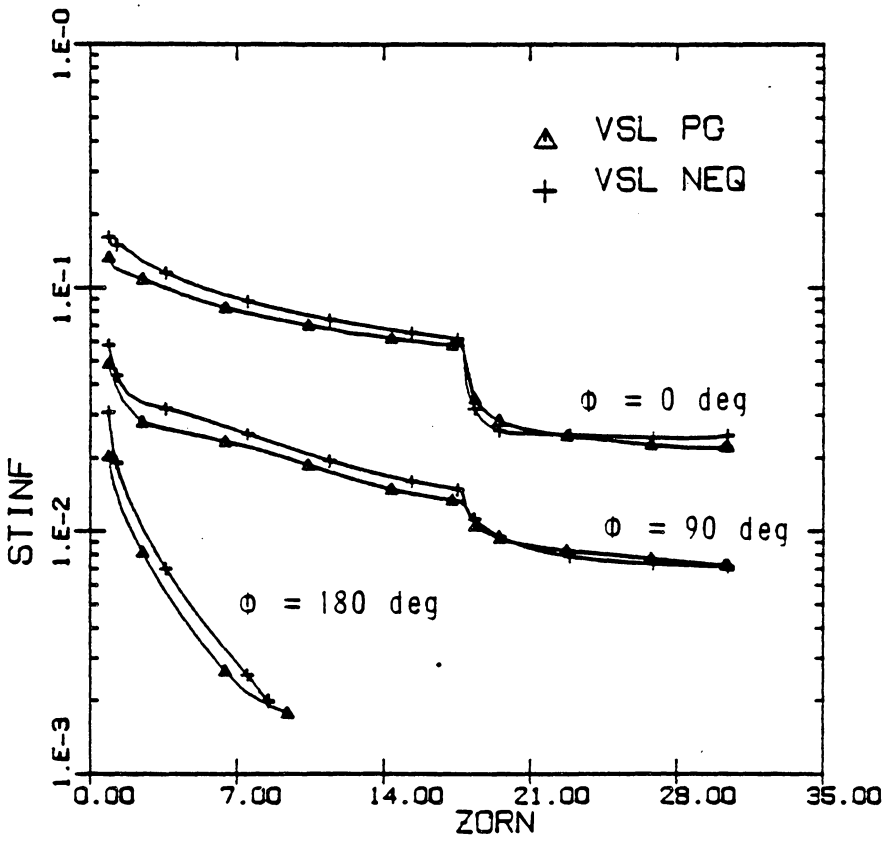

Fig.24. Surface heat-transfer distribution for Case 4 for α = 20 deg.

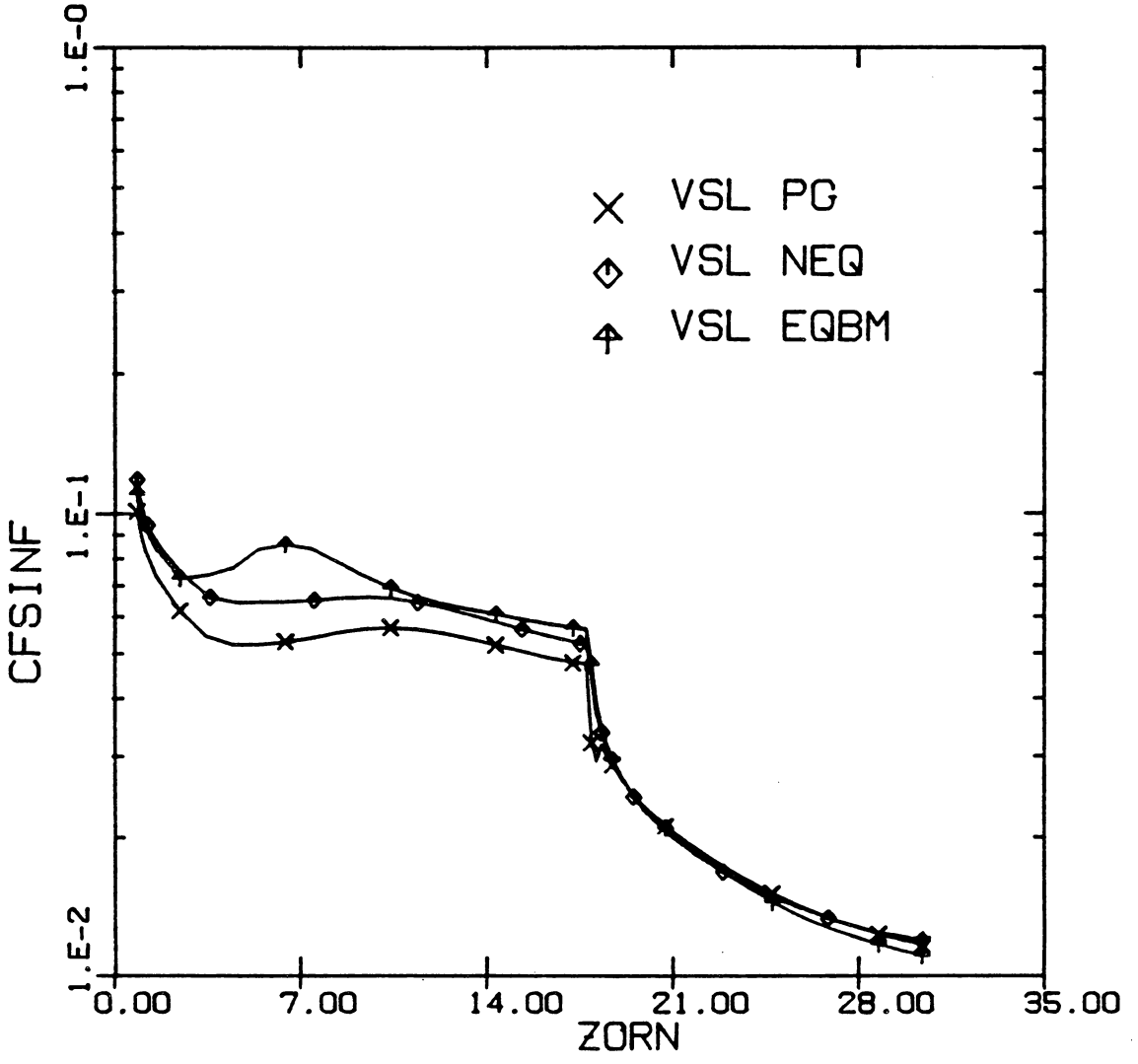

Fig.25a. Streamwise skin-friction distribution for Case 4 at α = 0 deg., ϕ = 0 deg.

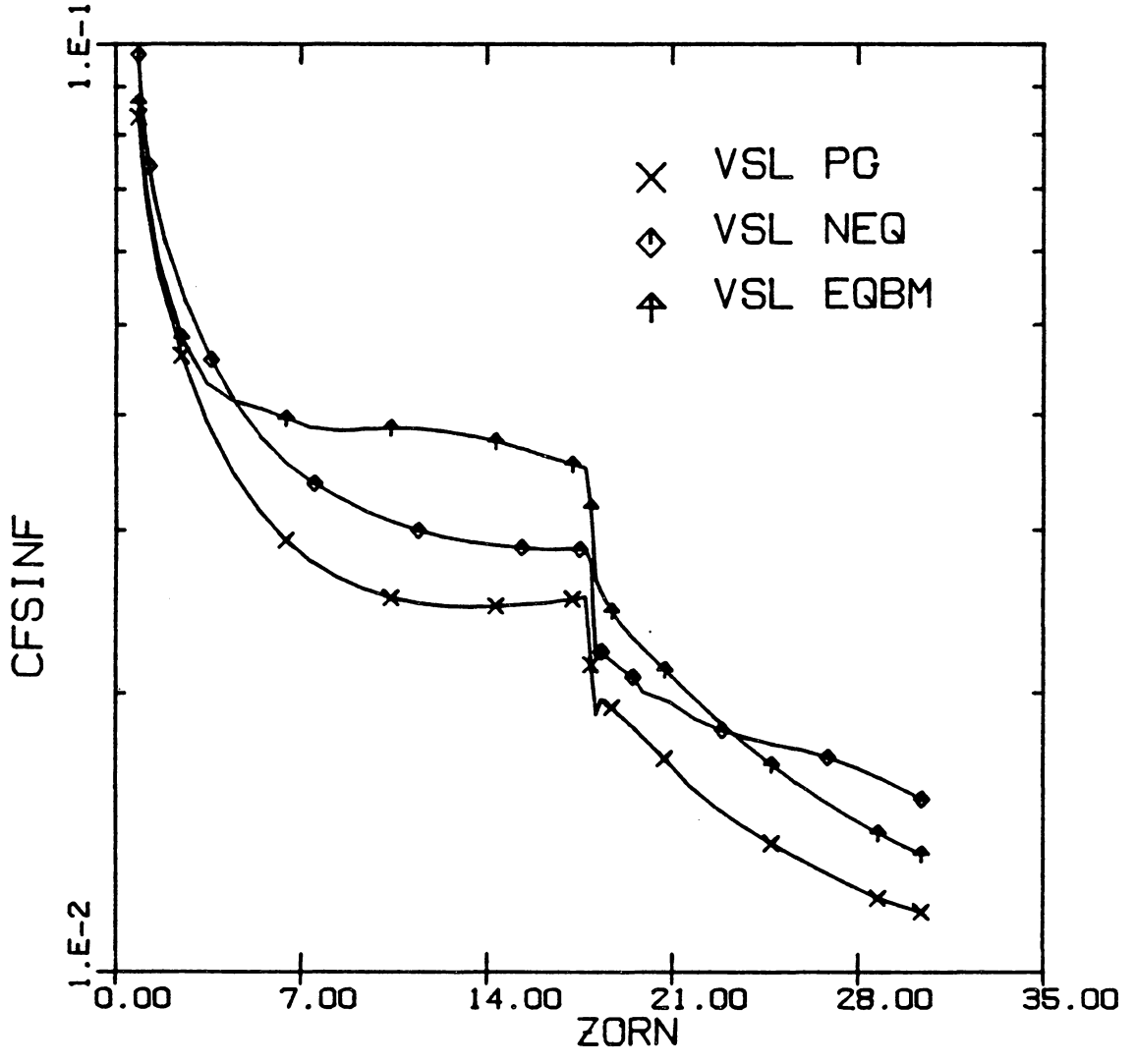

Fig.25b. Streamwise skin-friction distribution for Case 4 at α = 0 deg., ϕ = 90 deg.

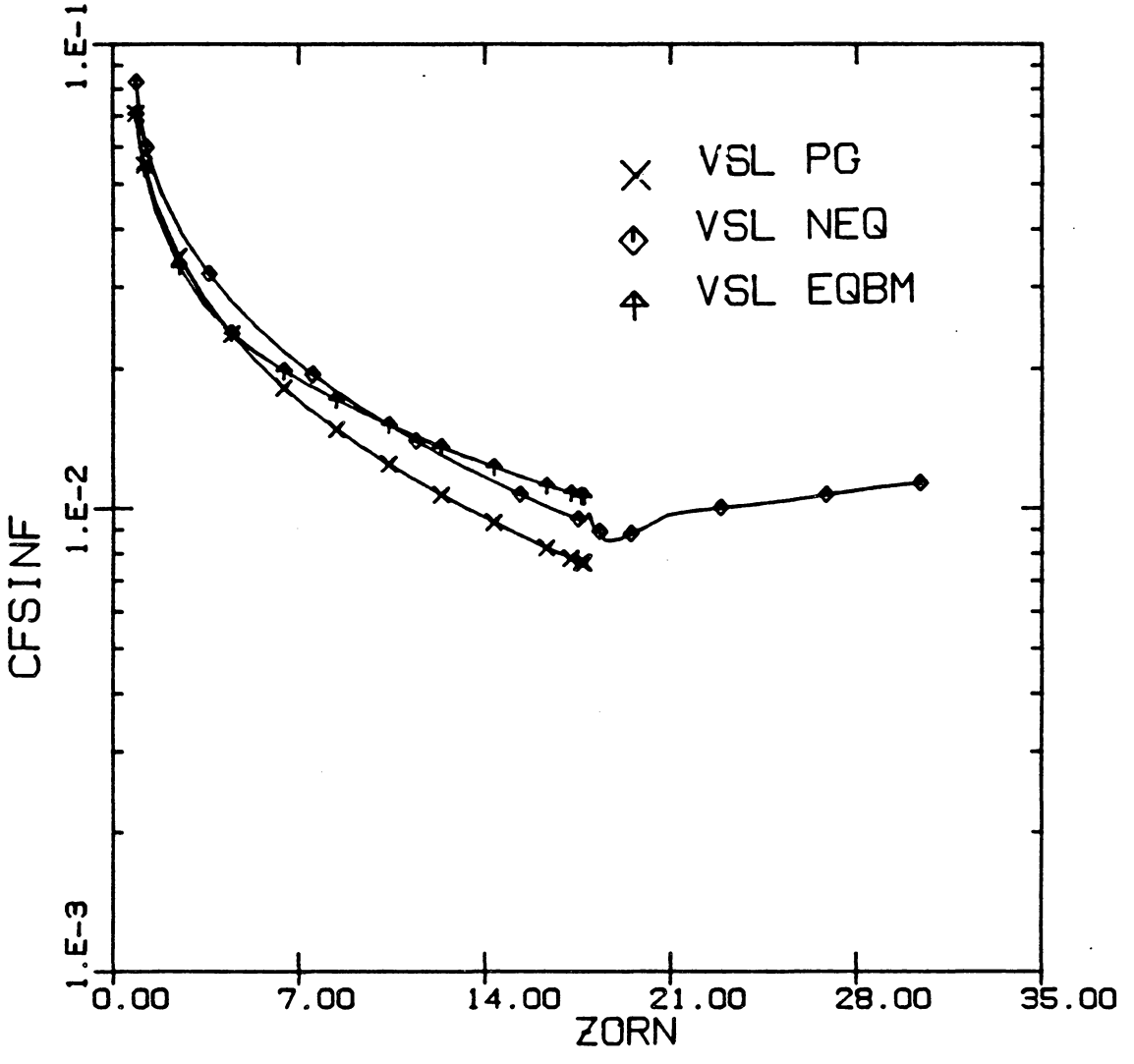

Fig.25c. Streamwise skin-friction distribution for Case 4 at α = 0 deg., ϕ = 180 deg.

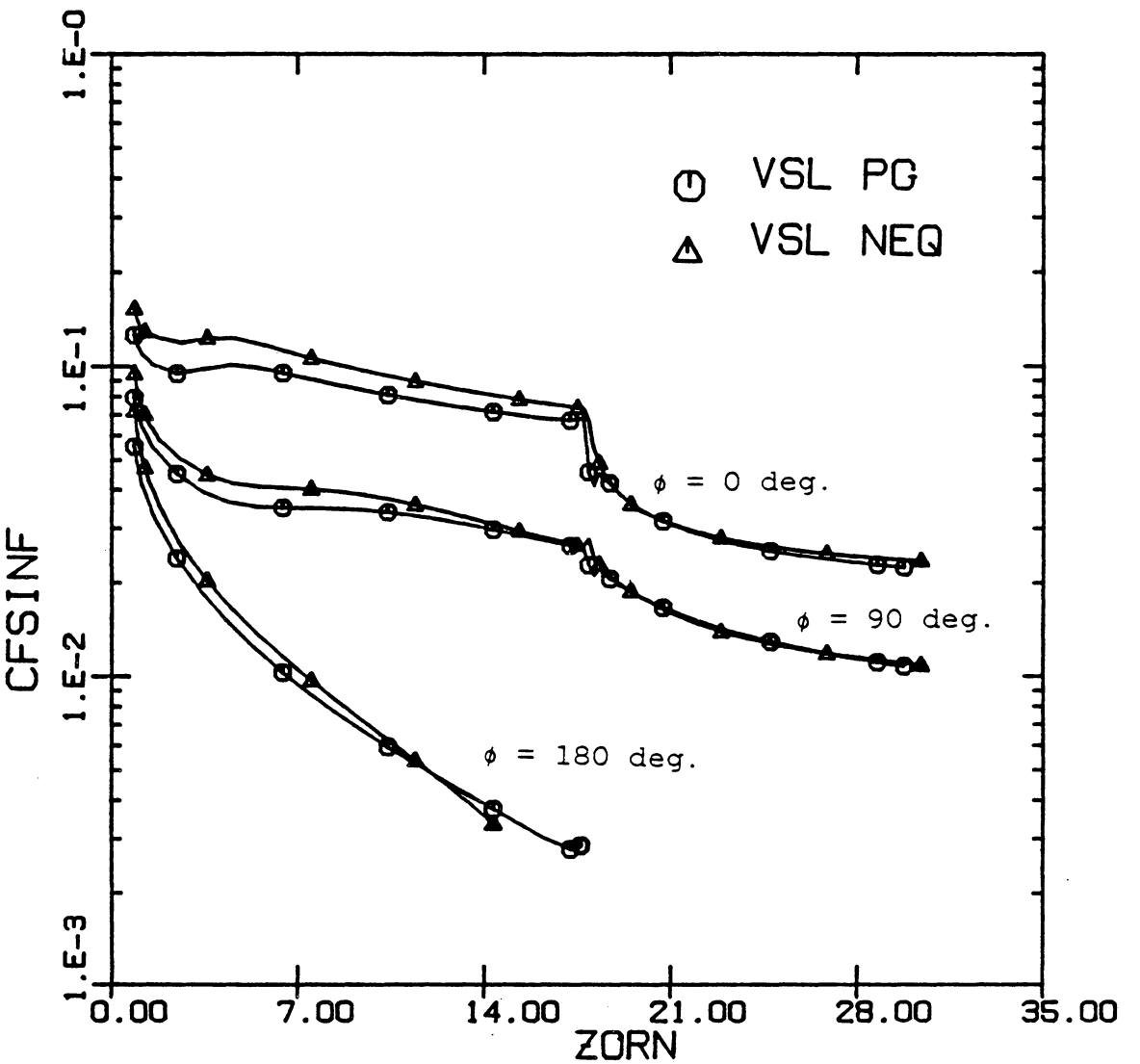

Fig.26. Streamwise skin-friction distribution for Case 4 for α = 10 deg.

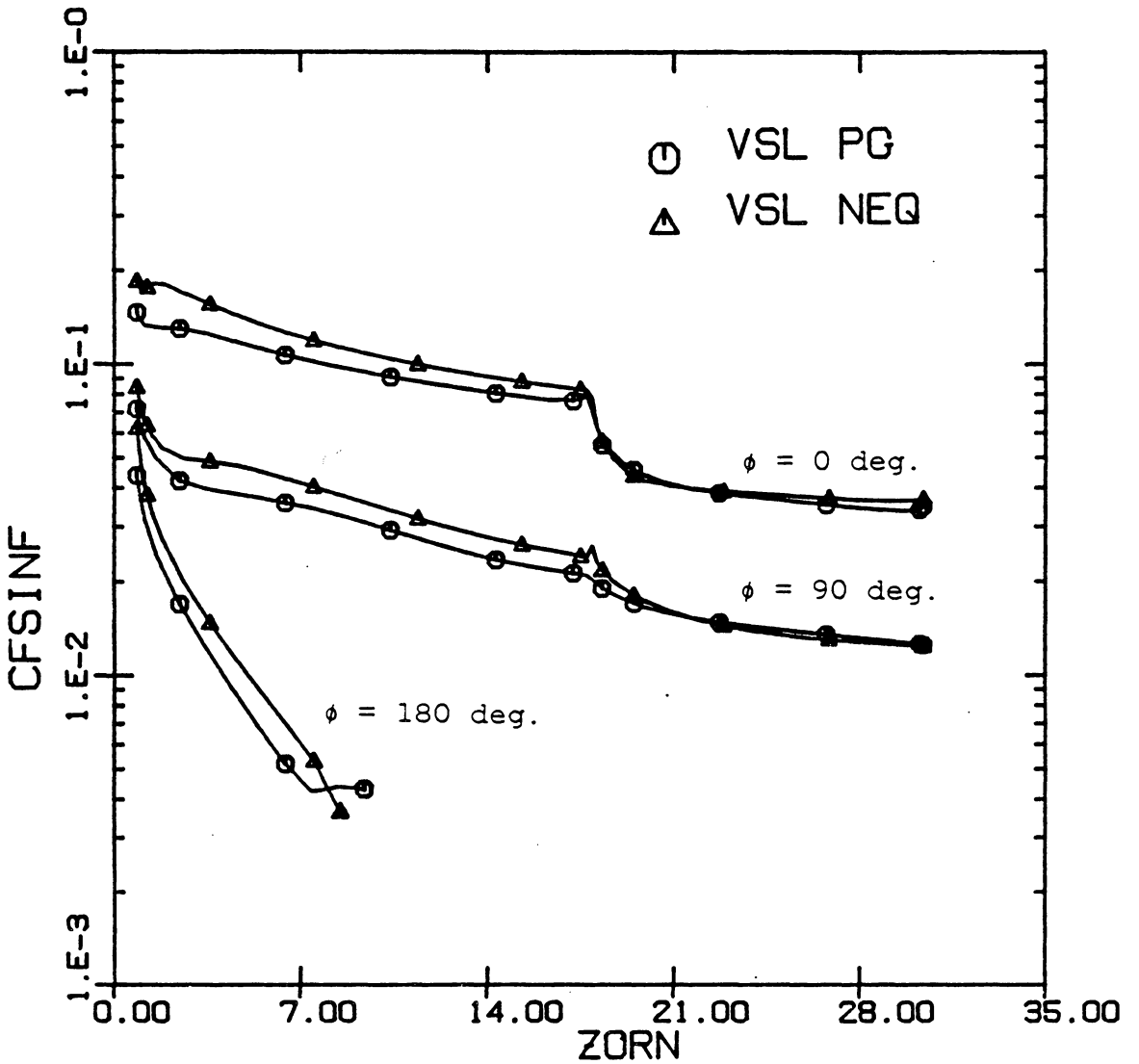

Fig.27. Streamwise skin-friction distribution for Case 4 for α = 20 deg.

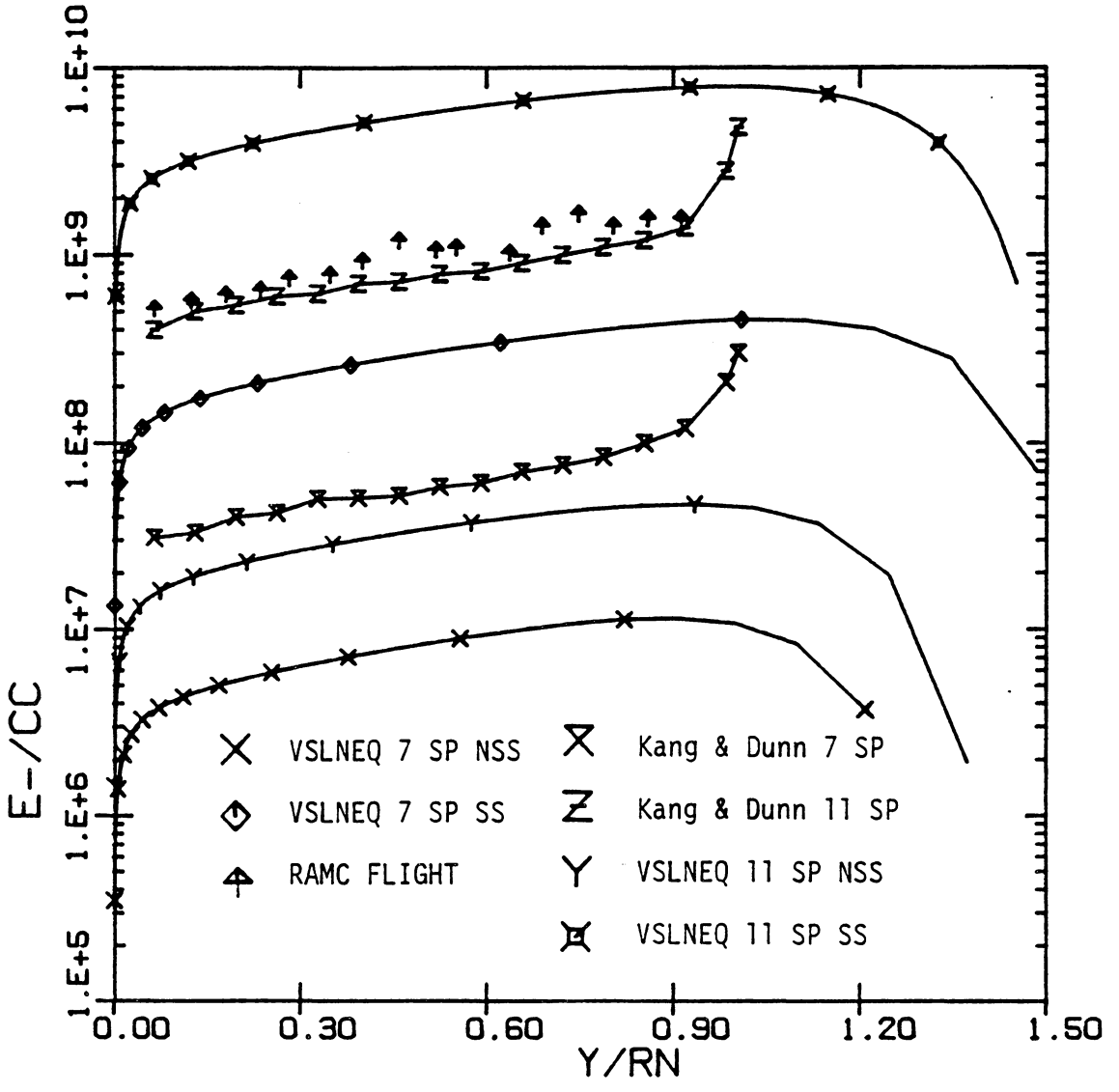

Fig.28. Effect of chemical models on electron number density for case 1 at s/Rn* = 8.8

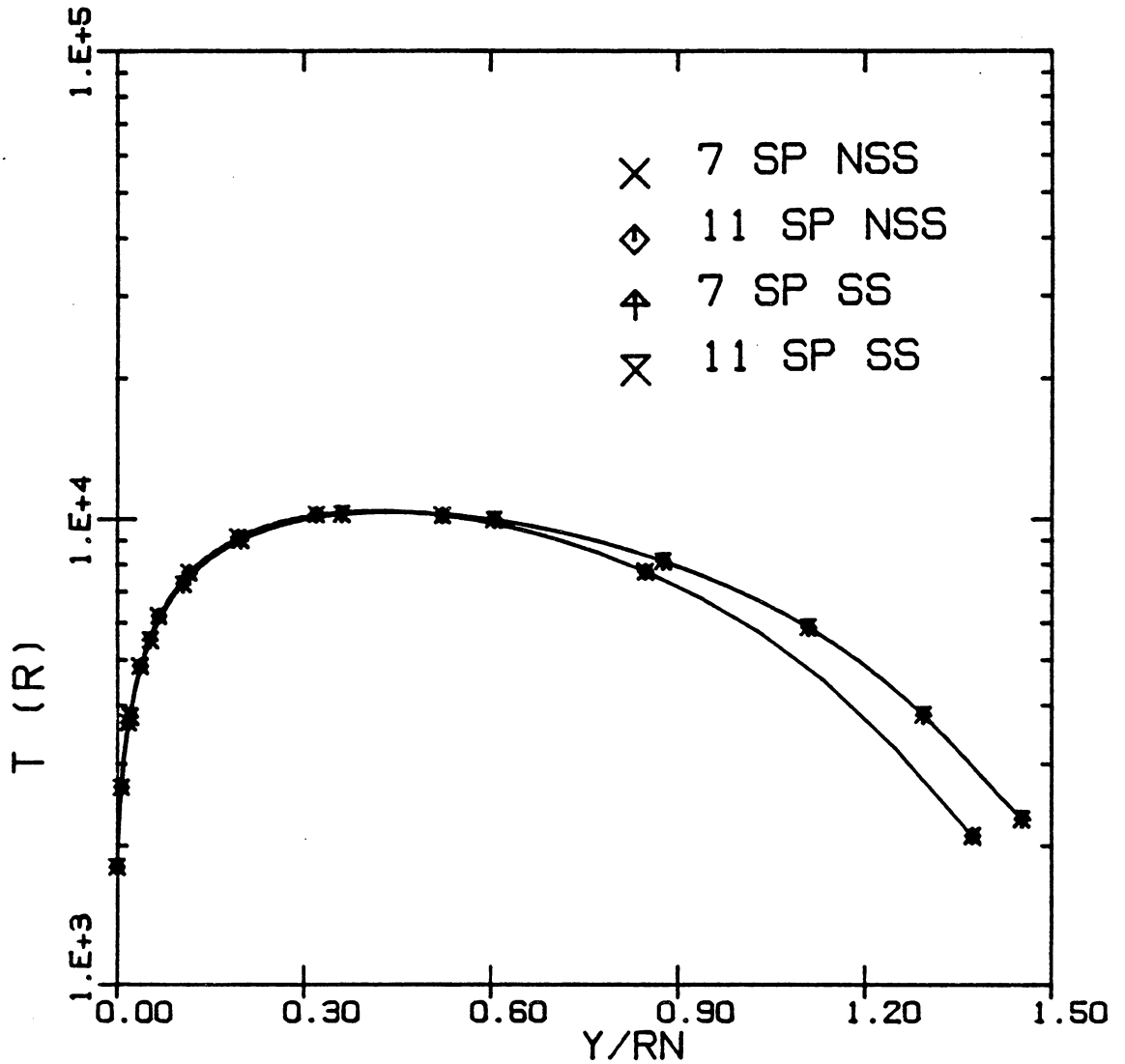

Fig.29. Shock-layer temperature profile for case 1 at s/Rn* = 8.8

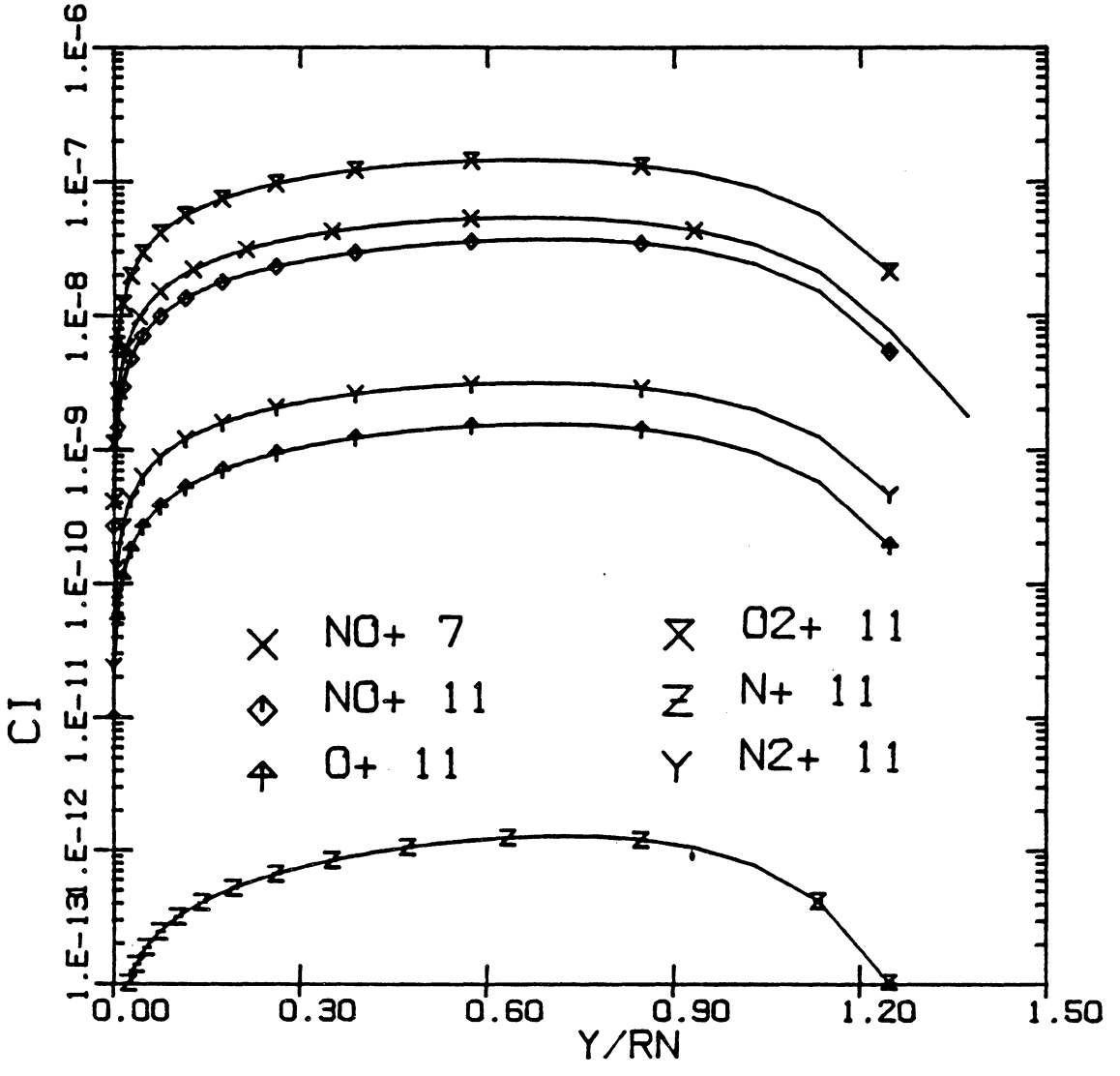

Fig.30. Concentration of ionized species for case 1 at s/Rn* = 8.8

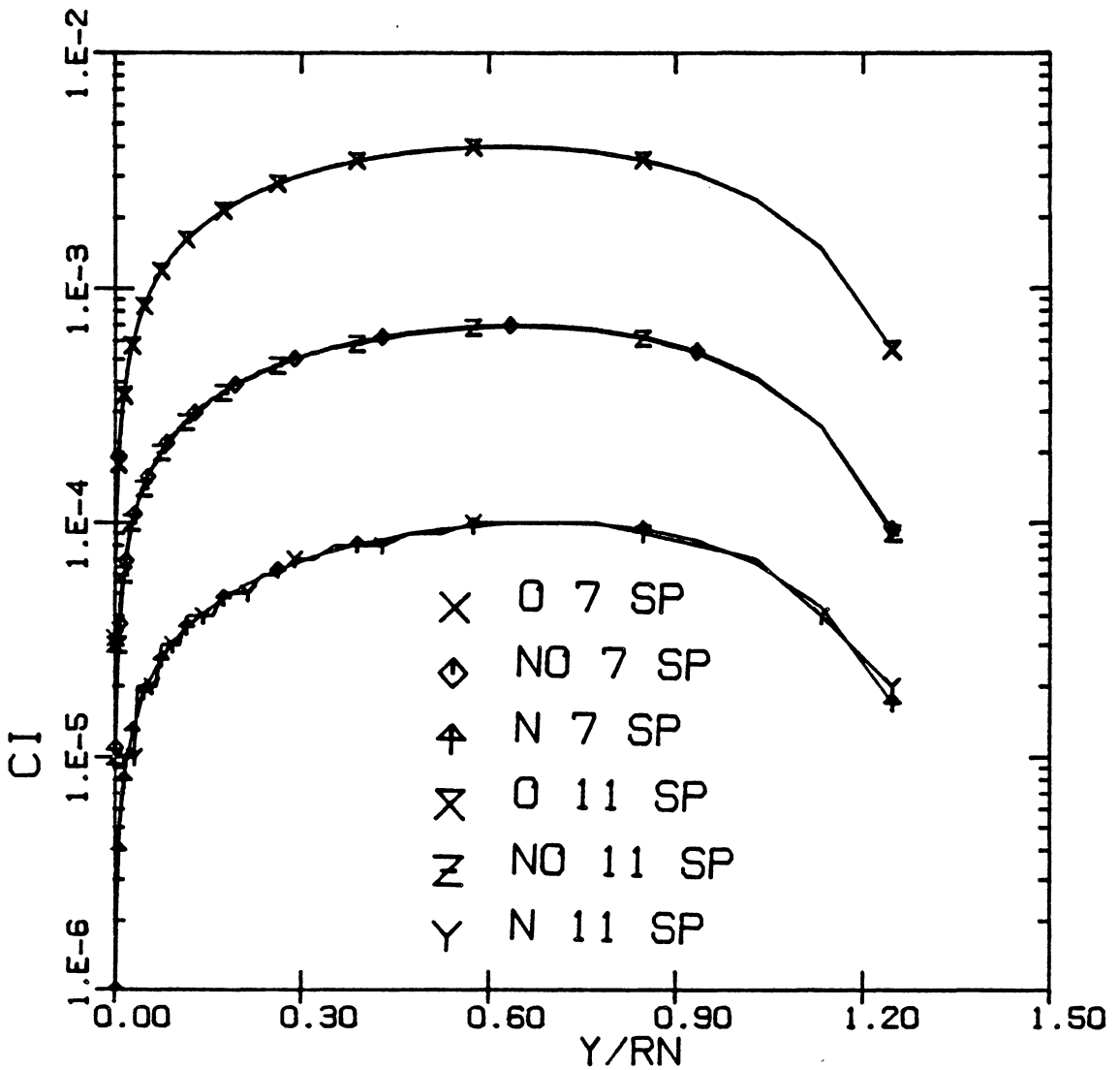

Fig.31. Concentration of dissociated species for case 1 at s/Rn* = 8.8

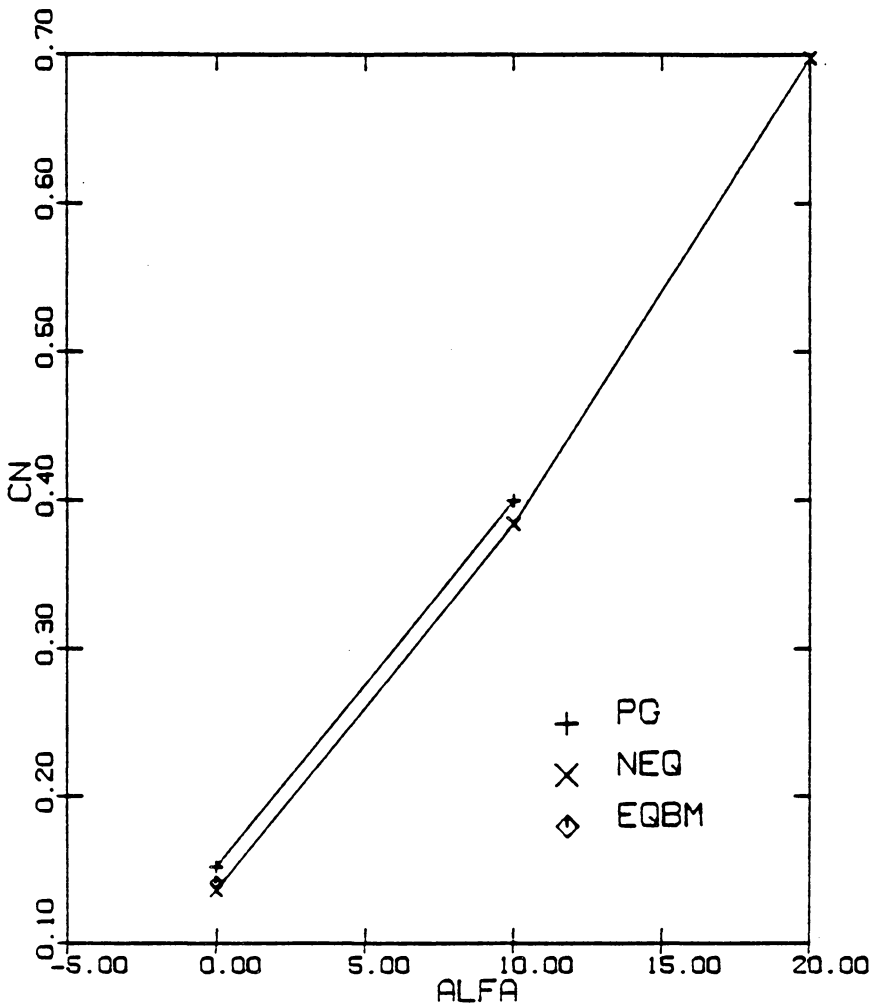

Fig.32. CN vs α for Case 4

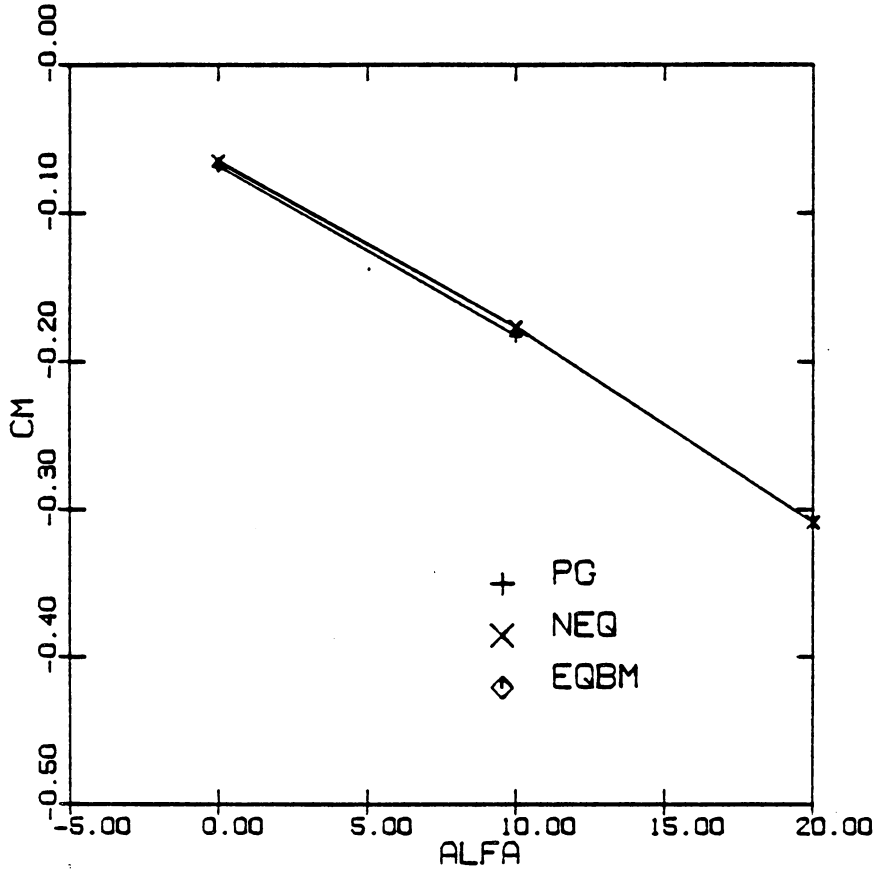

Fig.33. CM vs α for Case 4

The vita has been removed from the scanned document

THREE-DIMENSIONAL NONEQUILIBRIUM VISCOUS SHOCK-LAYER FLOWS OVER COMPLEX REENTRY VEHICLES

by

S. Swaminathan

(ABSTRACT)

A computer program for predicting the three-dimensional nonequilibrium viscous shock-layer flows over blunt sphere-cones, straight and bent multiconics at angle-of-attack has been developed. The method used is the viscous shock-layer approach for nonequilibrium, multi-component ionizing air. A seven species chemical reaction model with single ionizing species and an eleven species chemical reaction model with five ionizing species are used to represent the chemistry. The seven species model considers 7 reactions whereas the eleven species model considers 26, reactions and the results obtained using these models are compared with perfect gas and equilibrium air results. This code is capable of analyzing shock-slip or no-shock-slip boundary conditions and equilibrium or non-catalytic wall boundary conditions. In this study the diffusion model is limited to binary diffusion.

A sphere-cone-cylinder-flare with moderate flare angle, a straight biconic, and a bent biconic with seven deg. bend

angle and a sphere-cone at various flight conditions are analyzed using this method. The bent biconic has been analyzed up to an angle-of-attack of 20 deg. with respect to the aft-cone axis and sample results are compared with inviscid and viscous results. The surface pressure distribution computed by this code compares well with that from a parabolized Navier-Stokes method. The diffusion heat transfer is about 15% of the total heat transfer for most cases. The aerodynamic forces and moments at the base of the body and computing time required for all cases are presented. The shock layer profiles at a streamwise location of 8.8 nose radii for one case computed using seven and eleven species models compare very well with each other.